Qubit sensing by optimal narrowband pulses: Demonstration for Rabi frequency sensing

Meri Harutyunyan, Bruno Peaudecerf, Dominique Sugny, Stéphane Guérin

Qubit sensing by optimal narrowband pulses: Demonstration for Rabi frequency sensing

Meri Harutyunyan,[1] Bruno Peaudecerf,[2] Dominique Sugny,[1] and Stéphane Guérin[1,*]
[1]*Université Bourgogne Europe, CNRS, Laboratoire Interdisciplinaire Carnot de Bourgogne ICB UMR 6303, 21000 Dijon, France*
[2]*Laboratoire Collisions Agrégats Réactivité LCAR UMR 5589, CNRS, Université de Toulouse, 31000 Toulouse, France*

(Received 3 May 2025; accepted 28 October 2025; published 8 December 2025)

Narrowband optimal control is proposed as a protocol of optimal quantum sensing, providing maximum accuracy for given resources. The procedure is demonstrated on the IBM quantum computer to estimate the amplitude of the qubit Rabi frequency. It is based on optimizing the quantum Fisher information (QFI) when it becomes equal to the classical Fisher information. This scenario offers a practical quantum sensing because it only involves population transfer to the excited state as the target without dynamical phases, which would otherwise be difficult to control and measure. The protocol uses the single-shot-shaped pulse method and an inverse optimization, to design a pulse that results in the optimal QFI in terms of energy or equivalently operating time, referred to in short as local narrowband inverse optimization (NIO). Multiple π pulses are shown to be particular cases of this protocol. An alternative semiglobal optimal NIO procedure producing a partially nonoscillatory profile is also demonstrated. Our approach also offers application to optimal atomic selective excitation in an array of atoms for quantum technology.

DOI: 10.1103/gt51-g34c

I. INTRODUCTION

Quantum metrology or sensing is a cutting-edge technology offering high-resolution and high-sensitivity measurements, which is of paramount importance for quantum technologies [1–23]. Unlike traditional classical sensing methods, which collect data from a large number of systems, quantum sensing operates at the quantum level, providing highly precise information about various physical properties. Time-dependent Hamiltonians allow in principle precision beyond the limits imposed by time-independent Hamiltonians [24–26]. Techniques of shortcut to adiabaticity [27] and optimal control [28–31] have been proposed [32–34], aiming at maximizing the quantum Fisher information (QFI) [35,36]. Maximizing QFI means reaching its upper bound for given ressources. However, achieving such maximization by optimal protocols (i.e., by optimizing time or energy) may not be experimentally practical since the corresponding optimal state is in general a superposition of the bare states of the considered system with a specific dynamical phase, which is complicated to reach accurately, requiring precise controls, and, even more importantly, difficult to measure. On the contrary, classical Fisher information (CFI) [37], based on the projective measurement associated with the bare states, is a much more accessible quantity, but is intrinsically smaller than (or equal to) the QFI. Both requirements will be shown to be met for specific instances (multiple π pulses) where CFI is equal to QFI.

In this paper, we propose a procedure of quantum sensing that is based on the practical maximization of the QFI restricted to this situation for which CFI is equal to QFI. We consider the case of a qubit and a proof of principle of this procedure is demonstrated on IBM's quantum computer [38–40]. More specifically, the control protocol targets complete population transfer from the ground state of the qubit (referred to as CPT in short). The estimation of an unknown parameter consists in calculating the final dynamical state for a series of values of this parameter and a specific control pulse, and to check when the experimental result corresponds to the theoretical model. From the key property that a larger QFI is associated with a narrower fidelity profile with respect to this parameter, an optimized estimation corresponds to a profile that has the minimum width produced by minimum resources (time, energy, ...). Such profiles have been designed with (nonoptimal) composite pulses (CPs) in Ref. [41]. In this work, we show that one can reach maximum narrowband profiles from optimal control theory without any ansatz for the pulse parameters. This is achieved by the single-shot-shaped-pulse (SSSP) method [42] and inverse optimization, in short narrowband inverse optimization (NIO), based on the robust inverse optimization (RIO) technique [43], which leads on the contrary to broadband profiles. This will be shown to produce oscillatory profiles with several narrowband intervals. An alternative procedure featuring a partially monotonic nonoscillatory optimal profile is demonstrated. The protocol is applied for the sensing of the coupling of a two-state system (via its Rabi frequency), for which we show that the QFI is bounded by the square of the Rabi pulse area. The proof of principle is implemented on the IBM quantum computer via a digital version of NIO based on the digital RIO [44]. We remark that the link between this method and optimal control theory has been recently exhibited in Ref. [45].

Below, we provide the detailed structure of the paper and summarize its content in order to guide the reasoning that

*Contact author: sguerin@u-bourgogne.fr

allows one identifying sensing with optimal control, its characterization by QFI and CFI, and its practical implementation.

In Sec. II, we define the QFI, $\mathcal{F}_{\rm Q}(t)$, and CFI, $\mathcal{F}_{\rm C}(t)$, in the context of the two-state model (of Hamiltonian H_α) and highlight important properties. The QFI quantifies the instantaneous knowledge of the value of a parameter α and we provide its upper bound. We consider the specific problem of estimating the Rabi frequency defined as $(1+\alpha)\Omega$, where $\alpha = 0$ corresponds to an initial estimate. The goal consists then in determining the value of α with its precision. We show that it can be directly determined by the profile of the fidelity F of the CPT (obtained for a certain dynamics to be defined) as a function of α since the QFI represents its curvature [see Eq. (7)]: A larger QFI corresponds to a narrower profile, i.e., to a better knowledge of α. We show that the QFI attains its maximum bound (which is the square of the pulse area) when the dynamics follows (or quickly reaches) a half superposition of the eigenstates of $\partial_\alpha H_\alpha$, which corresponds in general to a superposition of the bare states. Since such a superposition is in practice difficult to control and to measure accurately, we limit the procedure to the particular situation corresponding to the dynamics achieving CPT, for which CFI is equal to QFI, i.e., the CFI reaches its maximum bound. We next present different strategies producing a narrowband CPT profile optimizing the energy. In terms of the resources, both CFI and QFI show in principle the same efficiency since both are bounded by the square of the pulse area for the considered sensing. This efficiency is achieved for a resonant pulse of $(2n+1)\pi$ area (with n a positive or null integer). We present its generalization with pulses of any other area (requiring a nonresonant pulse with a time-dependent detuning). We show that they produce an oscillatory profile, referred to as local profile, since the accurate sensing of α requires to be well located around $\alpha = 0$. The QFI in this case does not reach its maximum bound but approaches it as will be seen in Sec. III. An alternative strategy consists in flattening optimally the profile near the zero-area pulse, referred to as 0π pulse. This shows a monotonic nonoscillatory profile for $\alpha \leqslant 0$ referred to as semiglobal profile with a QFI below its maximum bound. We show that the composite pulse strategy [41] provides information values that scale only linearly with the pulse area (i.e., with the number of constituent pulses), far from the bound of the square of the pulse area.

In Sec. III, we present the principle of optimal quantum sensing, i.e., sensing by optimal control. The protocol uses the single-shot-shaped pulse method [42] combined with an inverse optimization [43], which is referred to as narrowband by NIO. Sections IV and V are devoted to its numerical demonstration and implementation on IBM's quantum computer, respectively. We conclude in Sec. VI. Additional material is provided in the Appendices.

II. QUANTUM AND CLASSICAL FISHER INFORMATION

A. Optimization of the quantum Fisher information

1. Definition of the quantum Fisher information

QFI, denoted as $\mathcal{F}_{\rm Q}(t)$, quantifies the instantaneous knowledge at time t of the value of a parameter α around a certain value α_0 associated with a Hamiltonian $H_\alpha(t)$ [35,37]. QFI can be expressed in a number of equivalent ways, as described in Appendix A. Here, we briefly introduce some expressions that will be used in the design of the control process and define the quantum sensing that we specifically address. These include Eq. (A10), with $t_i = 0$:

$$\mathcal{F}_{\rm Q}(t) = \frac{4}{\hbar^2}\left|\int_0^t \langle\phi_{\alpha_0}(s)|\partial_\alpha H_{\alpha_0}(s)|\phi_{\alpha_0,\perp}(s)\rangle ds\right|^2, \tag{1}$$

where $|\phi_{\alpha_0}(t)\rangle$ and $|\phi_{\alpha_0,\perp}(s)\rangle$ are, respectively, the state of a qubit when $\alpha = \alpha_0$ and its orthogonal state. The QFI can be shown to be bounded as [24,34]

$$\mathcal{F}_{\rm Q}(t) \leqslant \left[\frac{1}{\hbar}\int_0^t (\mu_{\max}(s) - \mu_{\min}(s))ds\right]^2, \tag{2}$$

where the $\mu_{\max}(t)$ and $\mu_{\min}(t)$ are the (instantaneous) maximum and minimum eigenvalues of the gradient $\partial_\alpha H_{\alpha_0}(t)$.

2. Quantum sensing of the Rabi frequency: Link between quantum control profile and QFI

We consider, as a typical quantum sensing problem, the estimation of the Rabi frequency of a qubit whose dynamics is governed by the Hamiltonian H_α that can be expressed in the basis $\{|0\rangle = [1,0]^\intercal, |1\rangle = [0,1]^\intercal\}$ as

$$H_\alpha = \frac{\hbar}{2}\begin{bmatrix} -\Delta & (1+\alpha)\Omega \\ (1+\alpha)\Omega & \Delta \end{bmatrix} = H_0 + \alpha\frac{\hbar\Omega}{2}\sigma_x, \tag{3}$$

where α is here a small relative (dimensionless) static parameter, $\alpha \ll 1$, to be determined, for which a first estimation defines H_0 (i.e., for $\alpha = \alpha_0 = 0$). Here, the Rabi frequency $\Omega \equiv \Omega(t)$ and the detuning $\Delta \equiv \Delta(t)$ are the time-dependent controls. Introducing the Euler angles $(\theta, \varphi, \gamma)$, we can parametrize the states (defined below for $\alpha = 0$ but the same form applies for any α) as

$$|\phi_0(t)\rangle = e^{-i\gamma/2}\begin{bmatrix} \cos(\theta/2)e^{i\varphi/2} \\ \sin(\theta/2)e^{-i\varphi/2} \end{bmatrix}, \tag{4a}$$

$$|\phi_{0,\perp}(t)\rangle = e^{i\gamma/2}\begin{bmatrix} -\sin(\theta/2)e^{i\varphi/2} \\ \cos(\theta/2)e^{-i\varphi/2} \end{bmatrix}. \tag{4b}$$

The Schrödinger equation can be expressed as a set of differential equations in terms of the Euler angles as [42]

$$\dot\theta = \Omega\sin\varphi, \tag{5a}$$

$$\dot\varphi = \Delta + \Omega\cos\varphi\cot\theta, \tag{5b}$$

$$\dot\gamma\sin\theta = \Omega\cos\varphi. \tag{5c}$$

Starting from the definition (1) and using Eq. (5), the QFI can be written as

$$\mathcal{F}_{\rm Q}(t) = \left|\int_0^t e^{i\gamma}\left[\frac{\dot\gamma}{2}\sin(2\theta) - i\dot\theta\right]ds\right|^2. \tag{6}$$

A key result is the relation between the QFI and the fidelity of the dynamics when $\alpha \neq 0$ with respect to the one when $\alpha = 0$. More precisely, we consider the fidelity, defined as $\mathsf{F}(t) = |\langle\phi_0(t)|\phi_\alpha(t)\rangle|^2$, where $|\phi_\alpha(t)\rangle$ is solution of the Schrödinger equation $i\hbar\frac{\partial}{\partial t}|\phi_\alpha(t)\rangle = H_\alpha|\phi_\alpha(t)\rangle$. It is shown in the next section that this fidelity is linked to the QFI for the CPT at second order of perturbation theory as follows [see

Eq. (D4)]:

$$\mathsf{F}(t) = |\langle\phi_0(t)|\phi_\alpha(t)\rangle|^2 = 1 - \frac{\alpha^2}{4}\mathcal{F}_\mathrm{Q}(t) + O(\alpha^3). \quad (7)$$

We then see that the QFI can be interpreted as the curvature of the fidelity F with respect to the parameter α: A larger QFI corresponds to a narrower profile. This result is intuitive in the sense that a narrower profile is associated with a better knowledge of the underlying parameter. A pulse $\Omega(t)$ [associated with a certain detuning $\Delta(t)$] achieving a narrowband profile is referred to as narrowband pulse.

The next tasks are to define the target state $|\phi_0(t)\rangle$ that will be used for *practical sensing* with large QFI (ideally maximum for given ressources), and how to optimally *reach* it.

3. Maximization of the QFI

The eigenvalues and eigenvectors of $\partial_\alpha H_\alpha = \hbar\Omega\sigma_x/2$ are $\pm\hbar\Omega/2$ and $|+\rangle = [1, 1]^\intercal/\sqrt{2}$, $|-\rangle = [1, -1]^\intercal/\sqrt{2}$, respectively. Introducing $\mathcal{A}(t) = \int_0^t \Omega(s)ds$ the area of the Rabi pulse, we obtain that the upper bound for the QFI is given by

$$\mathcal{F}_\mathrm{Q}(t) \leqslant \mathcal{A}(t)^2. \quad (8)$$

The optimal procedure that maximizes the QFI consists in reaching as fast as possible a balanced linear combination of the eigenstates (up to a global phase) $\frac{1}{\sqrt{2}}(|+\rangle + e^{i\vartheta}|-\rangle) = \frac{1}{\sqrt{2}}e^{i\vartheta/2}(e^{-i\vartheta/2}|+\rangle + e^{i\vartheta/2}|-\rangle)$ [associated with the perpendicular state $\frac{1}{\sqrt{2}}(e^{-i\vartheta}|+\rangle - |-\rangle) = \frac{1}{\sqrt{2}}e^{-i\vartheta/2}(e^{-i\vartheta/2}|+\rangle - e^{i\vartheta/2}|-\rangle)$] [24,34], since the QFI then reaches its bound:

$$\mathcal{F}_\mathrm{Q}(t) = \left|\int_0^t (\langle+| + e^{-i\vartheta}\langle-|)\partial_\alpha H_{\alpha_0}(s)(e^{-i\vartheta}|+\rangle - |-\rangle)ds\right|^2 = \mathcal{A}(t)^2. \quad (9)$$

In the expressions above, the angle ϑ is a relative phase of the superposition, which can take *a priori* any value for achieving Eq. (9).

This is performed for any transfer of state from the ground state by a resonant pulse, i.e., with a null detuning, for which we determine that $\vartheta = \mathcal{A}$ (see Sec. II C 1). However, such superposition is expected to be complicated to reach accurately and, even more importantly, difficult to measure. In practice, this means that the target state associated with the maximum bound of the QFI is generally a superposition of states of the system, which may not be accessible experimentally or difficult to access.

A particularly important and *practical* case is a π-pulse CPT, for which $\vartheta = \mathcal{A} = \pi$, or any integer of π pulse (CPT for an odd number of π or population return for an even number of π), where only a bare state (excited or ground state) is involved and has to be measured.

B. Classical Fisher information: Definition and conditions of maximization

The measurement precision is bounded by the QFI. This bound corresponds to a specific positive operator-valued measure (POVM) to be used in the estimation process [37]. In a given experimental setup, this limit may not be reached if this POVM is not available. This difficulty can be circumvented by considering the CFI, denoted as $\mathcal{F}_\mathrm{C}$, which is defined directly from the experimental POVM. By construction, we have

$$\mathcal{F}_\mathrm{C} \leqslant \mathcal{F}_\mathrm{Q}. \quad (10)$$

We introduce the CFI associated with the projection-valued measure (PVM) $\{|0\rangle\langle 0|, |1\rangle\langle 1|\}$, which is defined as [37]

$$\mathcal{F}_\mathrm{C} = \sum_{k=0}^{1} \frac{\left(\frac{d}{d\alpha}|\langle k|\phi_\alpha\rangle|^2\right)^2}{|\langle k|\phi_\alpha\rangle|^2}. \quad (11)$$

This corresponds to the measurement of populations in the ground/excited states, which is usually the most easily accessible in experiment.

In Appendix B, we provide an alternative expression of the CFI and establish the following property:

If $|\phi_0\rangle = |0\rangle$ *or* $|1\rangle$, then $\mathcal{F}_C = \mathcal{F}_Q$ in the limit of small α.

We will then consider the situation of CPT for which the CFI reaches the QFI and is maximum.

C. Strategies of sensing optimization by CPT profiles

We summarize in this section several control strategies to maximize the CFI for sensing, i.e., using a CPT profile, which will be investigated in the next sections. We thus assume that the initial state (at $t_i = 0$) is the ground state $|0\rangle$.

1. Resonant pulses are optimal local narrowband pulses

For the resonant dynamics (i.e., with $\Delta = 0$), we have for the state [Eq. (4a)] $|\phi_0\rangle = [\cos(\frac{1}{2}\theta(t)), -i\sin(\frac{1}{2}\theta(t))]^\intercal$ with the pulse area $\mathcal{A}(t) = \theta(t) = \int_0^t \Omega(s)ds$ and the phases $\varphi(t) = \gamma(t) = \frac{\pi}{2}$, and $|\phi_{0,\perp}\rangle = [-i\sin(\frac{1}{2}\theta(t)), \cos(\frac{1}{2}\theta(t))]^\perp$. We deduce that

$$|\partial\phi\rangle = \frac{\theta(t)}{2}\begin{bmatrix} -\sin\left(\frac{1}{2}\theta(t)\right) \\ -i\cos\left(\frac{1}{2}\theta(t)\right)\end{bmatrix} = -i\frac{\theta(t)}{2}|\phi_{0,\perp}\rangle, \quad (12)$$

i.e., $c = -i\frac{\theta(t)}{2}$ and thus $\varphi_c = -\frac{\pi}{2}$ and $\varphi_c + \gamma = 0$. We conclude (from Appendix B) that the resonant dynamics maximize both the CFI and QFI at all times, with

$$\mathcal{F}_\mathrm{C}(t) = \mathcal{F}_\mathrm{Q}(t) = \mathcal{A}(t)^2. \quad (13)$$

This shows the quadratic scaling of the QFI/CFI as a function of the pulse area.

As mentioned above, in order to avoid the measurement of superposition of states in practice, we consider the sensing protocol defined through the excitation profile (or fidelity) $\mathsf{F} \equiv \mathsf{F}_\mathrm{CPT} = |\langle 1|\phi_\alpha(t_f)\rangle|^2$, i.e., with the choice $|\phi_0\rangle \equiv |1\rangle$ (up to a phase) at a final time t_f in Eq. (7). The curvature around the CPT (i.e., the QFI) is given by

$$\mathcal{F}_{\mathrm{C},(2n+1)\pi} = \mathcal{F}_{\mathrm{Q},(2n+1)\pi} = (2n+1)^2\pi^2, \quad (14)$$

with $n \geqslant 0$ an integer. The number of π pulses in the area is here characterized by the number $2n+1$. The π-pulse resonant dynamics is the optimal pulse achieving CPT (with respect to pulse area, or with respect to time or energy for a square pulse) [46]. It gives the CFI and QFI [Eq. (14)] with $n = 0$. By extension, we will obtain that the multiple $(2n+1)\pi$ pulse resonant dynamics is the optimal pulse for the estimation of the parameter α with the CFI and QFI given

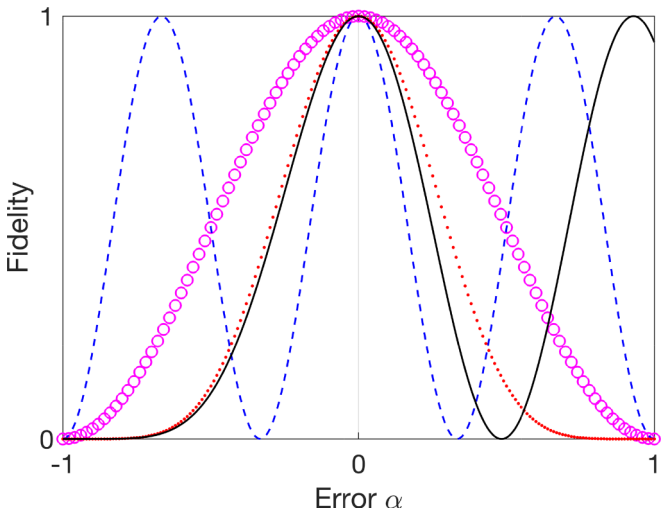

FIG. 1. Excitation profile (or fidelity) $\mathsf{F}_{\mathrm{CPT}} = |\langle 1|\phi_\alpha\rangle|^2$ as a function of the pulse amplitude error α exhibiting the QFI as its curvature around $\alpha = 0$ for (1) a π pulse (magenta circle line) and a 3π pulse (dark blue dashed line, also referred to as QFI-NOP pulse for $\mathcal{F}_{\mathrm{Q}} = 9\pi^2$), showing an (oscillatory) locally narrowband profile for a multiple π pulse; (2) the 3π composite pulse (red dotted line) featuring a global (nonoscillatory) narrowband profile, however, of lower QFI ($\mathcal{F}_{\mathrm{Q}} = 3\pi^2$) than the resonant 3π pulse; and (3) the optimal 0π-NOP of fifth order (of 2.435π pulse area and $\mathcal{F}_{\mathrm{Q}} \approx 3.67\pi^2$) (black full line), exhibiting a semiglobal narrowband profile (i.e., nonoscillatory for $\alpha < 0$). The latter shows a 20% better QFI than the composite pulse for a 20% lower pulse area.

by Eq. (14), i.e., that are maximum for the given pulse areas $\mathcal{A} = (2n+1)\pi$.

The respective excitation profiles for the 3π and 5π pulses as a function of the error α in the single-pulse area are shown in Figs. 1 and 2. The improvement of the narrowness for a larger number of multiple π pulses is clearly observed. One can notice that the $(2n+1)\pi$-pulse profile oscillates with $2n+1$ peaks in the interval $\alpha \in [-1, 1]$.

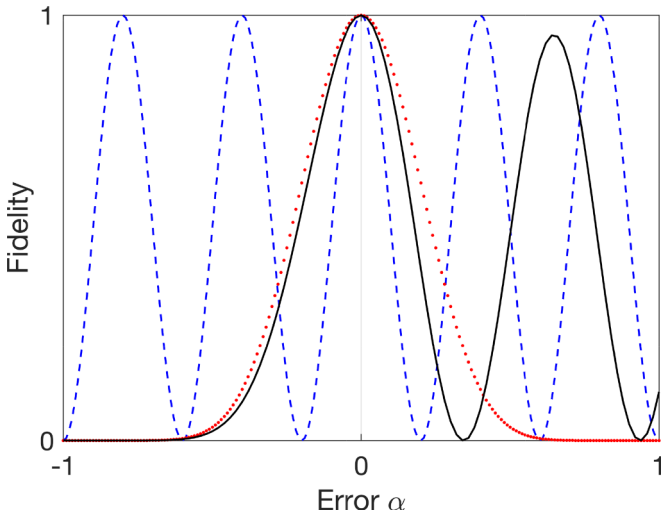

FIG. 2. Same as Fig. 1 but for a 5π pulse (dark blue dashed line), the 5π composite pulse (red dotted line), and the (semiglobal) optimal 0π-NOP of ninth order (of 3.81π pulse area and $\mathcal{F}_{\mathrm{Q}} \approx 6.87\pi^2$) (black full line). The latter shows a 37% better QFI than the composite pulse for a 24% lower pulse area.

2. Generalization of optimal local narrowband pulses

We will design the optimal pulse (in amplitude and phase) that reaches a given $\mathcal{F}_{\mathrm{Q}} = \mathcal{F}_{\mathrm{C}}$, anywhere in the intervals between the multiple π pulse given by Eq. (14). The resulting profile of the fidelity [Eq. (7)] will be shown to be narrowband, but in general oscillatory as for the multiple π pulse (being particular cases of such optimal pulses). Such pulses as well as the resonant $(2n+1)\pi$ pulse produce thus *optimal local narrowband fidelity profiles*, and are referred to in short as *QFI-NOP* pulses. Contrary to the $(2n+1)\pi$ pulses, such pulses do not lead in general to the maximum bound for the QFI but approach it. We remark that the presence of multiple peaks can lead to inaccurate sensing, which occurs if a wrong peak is targeted.

3. Global narrowband composite pulses

An alternative strategy using CP has been proposed in Ref. [41]. A sequence of a odd number $N = 2n+1$ of π pulses with sign-alternating phases $\phi_k^{(N)} = k\pi/N$, $k = 2, 4, 6, \ldots, N-1$, and $\phi_k^{(N)} = -(k-1)\pi/N$, $k = 1, 3, 5, \ldots, N$, leads to the excitation probability $p = \sin^{2N}(A/2)$, where A is the area of a single pulse: $\mathcal{A} = NA$. This features a flat profile around the 0π single pulse, i.e., $\alpha = -1$ (and around the 2π single pulse, i.e., $\alpha = 1$) behaving monotonically from 0π single pulse (no transfer) to π single pulse (CPT). It has been shown to lead to a narrowband profile around $\alpha = 0$. Expanding the single-pulse area around π, $A = \pi(1+\alpha)$, we can then derive the QFI and show that it scales only linearly as a function of the total pulse area:

$$\mathcal{F}_{\mathrm{Q},(2n+1)\mathrm{CP}} = (2n+1)\pi^2, \tag{15}$$

which is much less efficient than the quadratic scaling [Eq. (14)] obtained for multi-π pulses.

The 3π and 5π CP narrowband fidelity profiles are shown in Figs. 1 and 2, respectively. They both feature a single peak and are thus referred to as *global narrowband* compared to the oscillating profiles produced by multi-π pulses.

4. Optimal semiglobal narrowband pulses

Inspired by the result from the narrowband composite pulses, we will develop the strategy that flattens the profile at $\alpha = -1$, which remarkably leads to a partially nonoscillatory narrowband profile (for $\alpha \leqslant 0$), but in an optimal way, i.e., an *optimal semiglobal narrowband profile*. The pulses producing such profiles are referred in short to as 0π-NOP pulses. The fidelity profiles are shown in Figs. 1 and 2 for the respective fifth and ninth orders. Such pulses do not lead to the maximum bound for the QFI, but are still superior to the CP pulses (see Fig. 5).

We notice that this strategy has also the technical advantage that derivatives of higher orders can be addressed directly by nullifying each of them.

III. OPTIMAL QUANTUM SENSING: THEORY

Our protocol is based on an optimal control leading to a narrowband CPT fidelity profile for a given QFI equal to CFI. As already mentioned, we consider CPT since the curvature of the profile can be measured conveniently without involving any superposition of bare states. We remark that our control process does not directly maximize QFI, nor CFI, because the final state is fixed. It will be however shown numerically that the obtained QFIs are close to their theoretical upper bound. Optimality refers to the shortest (minimum) time, to the least energy-consuming way, or to the smallest pulse area (depending in general on the chosen cost) that reaches a given QFI. In the situation that is considered, the estimation of the coupling term via the Rabi frequency, the optimal protocol gives the same solution for the three costs (time, energy, or pulse area minimum) since there is no drift term in the Hamiltonian [46].

Both narrowband QFI-NOP and 0π-NOP pulses can be generated by the SSSP method [42] combined with an inverse optimization [43], referred to as NIO in this context, as shown below and in the Appendices.

A. The Single-Shot-Shaped Pulse method

Both optimal broadband (robust) and narrowband controls can be implemented with the use of the SSSP method [42], which is introduced below and in Appendix C.

The knowledge of the control parameters $\Omega(t)$ and $\Delta(t)$ gives us the dynamics of the qubit. The reverse is also true: By inverting Eq. (5), we can determine the control $\Omega(t)$ and $\Delta(t)$ from the knowledge of two dynamical variables among the three angles $\theta(t)$, $\varphi(t)$, $\gamma(t)$:

$$\Delta = \dot{\varphi} - \dot{\gamma}\cos\theta, \tag{16a}$$

$$\Omega = \sqrt{\dot{\theta}^2 + \dot{\gamma}^2 \sin^2\theta}. \tag{16b}$$

Choosing, e.g., the given dynamical angles $\theta(t)$, $\gamma(t)$, one can indeed determine $\varphi(t)$ from Eq. (5c) (assuming $\Omega > 0$):

$$\varphi = \arctan\left(\frac{\dot{\theta}}{\dot{\gamma}\sin\theta}\right), \quad \begin{cases} 0 \leqslant \varphi \leqslant \pi, & \text{for } \dot{\theta} \geqslant 0, \\ -\pi < \varphi < 0, & \text{for } \dot{\theta} < 0. \end{cases} \tag{17}$$

For the control of CPT, the boundary values are $\theta_i = 0$, $\theta_f = \pi$, and $\gamma_i = \varphi_i$. From Eq. (5c), it follows that $\varphi_i = \varphi_f = \pi/2$.

More generally, one can consider any target state, and even any state defined by the dynamics of $H_0(t)$. We thus formulate the perturbative expansion considering the fidelity between the state solution $|\phi_\alpha(t)\rangle$ of $H_\alpha(t)$ with respect to the one $|\phi_0(t)\rangle$ of $H_0(t)$, i.e., for $\alpha = 0$, at the same time t:

$$\langle\phi_0(t)|\phi_\alpha(t)\rangle = 1 + O_1 + O_2 + O_3 + \cdots, \tag{18}$$

with the order of the perturbation $O_n \equiv O(\alpha^n)$, where $\alpha \ll 1$ represents the small parameter. The shape of the profile around $\alpha = 0$ is controlled via the respective terms $O_n \equiv O(\alpha^n)$. They have to be nullified for robust control or made on the contrary large for narrowband control.

The perturbative expansion at the heart of the method is detailed in Appendix C. It provided the explicit form of the corrections $\widetilde{O}_n$ [see Eq. (C6)] of the fidelity

$$\mathsf{F}(t) := |\langle\phi_0(t)|\phi_\alpha(t)\rangle|^2 = 1 + \widetilde{O}_1 + \widetilde{O}_2 + \widetilde{O}_3 + \cdots. \tag{19}$$

B. Narrowband profile by QFI-NOP

Producing an optimal narrowband profile means shaping a pulse that minimizes the energy or equivalently the pulse area, or the time of operation, leading to a given narrowband profile of the fidelity as a function of the parameter to be determined, here α. This strategy consists more specifically to target a given QFI of the profile around $\alpha = 0$, for which the optimal pulse is referred to as the QFI-NOP pulse. The technique is developed in Appendix D, where the Euler-Lagrange equations are derived and lead to the differential equations for the trajectory $(\gamma(t), \theta(t))$ that has to be minimized (with respect to its corresponding energy):

$$0 = \ddot{\gamma} + 2\dot{\gamma}\dot{\theta}\cot\theta + \dot{\theta}(\lambda_1 \sin\gamma - \lambda_2\cos\gamma), \tag{20a}$$

$$0 = \ddot{\theta} - \tfrac{1}{2}\dot{\gamma}^2 \sin 2\theta - \dot{\gamma}\sin^2\theta(\lambda_1\sin\gamma - \lambda_2\cos\gamma). \tag{20b}$$

Inverse optimization means that we next derive the controls $\Omega(t)$ and $\Delta(t)$ from the trajectories $\gamma(t)$ and $\theta(t)$ obtained as solutions of Eq. (20). By combining Eqs. (20a) and (20b) to substitute the term with the Lagrange multipliers, we get the constant of motion corresponding to a constant pulse $\Omega \equiv \Omega_0 = \text{cst.}$ with $|\dot{\theta}_i| = \Omega_0 > 0$, which is used as the normalization of the Lagrangian multipliers $\lambda_j = \tilde{\lambda}_j\Omega_0$, $j = 1, 2$ and the time $t = \tilde{t}/\Omega_0$. We obtain $\dot{\gamma}_i = 0$ from Eq. (20a) at the initial time $t_i = 0$. In summary, the boundaries, including CPT, to be considered read

$$\gamma_i = \frac{\pi}{2}, \ \dot{\gamma}_i = 0, \ \theta_i = 0, \ \theta_f = \pi, \ |\dot{\theta}_i| = \Omega_0. \tag{21}$$

In order to derive the form of the detuning as a function of the trajectory and for a constant Ω, we substitute $\dot{\varphi}$ from the derivation of Eq. (5c) $\ddot{\gamma}\sin\theta + \dot{\gamma}\dot{\theta}\cos\theta = -\dot{\varphi}\Omega_0\sin\varphi = -\dot{\varphi}\dot{\theta}$ into Eq. (16a):

$$\Delta = -\frac{1}{\dot{\theta}}(\ddot{\gamma}\sin\theta + 2\dot{\gamma}\dot{\theta}\cos\theta) = \sin\theta(\lambda_1\sin\gamma - \lambda_2\cos\gamma), \tag{22}$$

where we have used Eq. (20a) for the last equality. Each trajectory solution of Eq. (20) satisfying the boundary conditions (21), obtained for certain Lagrangian parameters, will provide an optimal pulse associated with a certain QFI. This will be numerically analyzed in the next section (see Fig. 3). The QFI will be shown to vary closely to its quadratic maximum as a function of the pulse area (see Fig. 5).

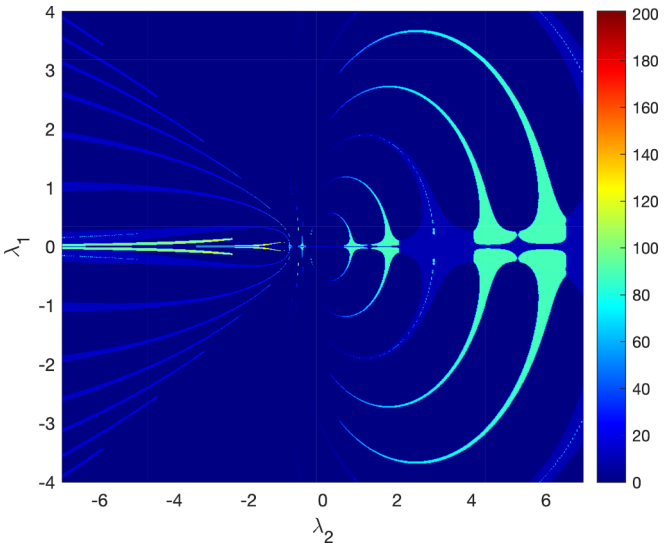

FIG. 3. Landscape as contour plot of the (dimensionless) QFI from the solution of the differential Eq. (20) as a function of the two Lagrangian multipliers (in units of Ω_0) (QFI-NOP). Dark blue color corresponds to absence of complete transfer (i.e., QFI artificially set at zero), while lighter color indicates a larger QFI, i.e., a narrower profile, when CPT is achieved.

C. Narrowband profile by 0π-NOP

For this strategy, we introduce $\varepsilon \equiv \alpha + 1 \to 0^+$ for $\alpha \to -1$ and redefine the decomposition of the Hamiltonian (3)

$$H_{\alpha\to -1} = \frac{\hbar}{2}\begin{bmatrix} -\Delta & 0 \\ 0 & \Delta \end{bmatrix} + \frac{\varepsilon\hbar}{2}\begin{bmatrix} 0 & \Omega \\ \Omega & 0 \end{bmatrix} \equiv H_\Delta + \varepsilon V. \quad (23)$$

The corresponding Euler-Lagrange equations at fifth order are determined in Appendix E. We obtain the four differential

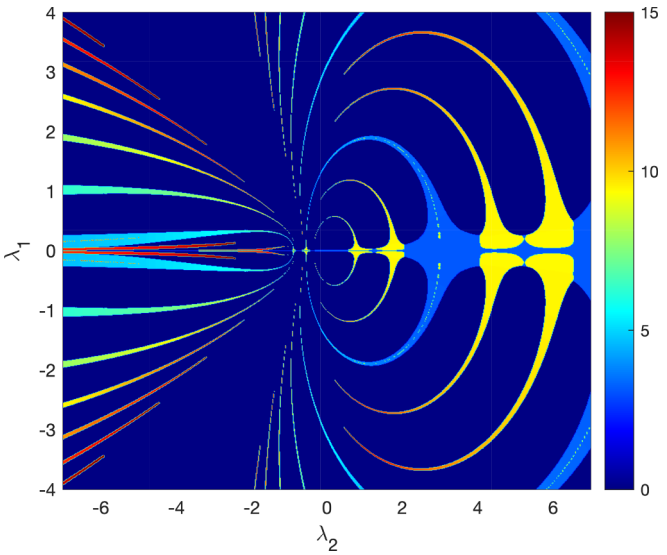

FIG. 4. Contour plot of the (dimensionless) pulse area as a function of the two Lagrangian multipliers (in units of Ω_0) from the solutions in Fig. 3. Dark blue color corresponds to absence of complete transfer (i.e., area artificially set as zero), while lighter colors indicate larger pulse areas when CPT is achieved.

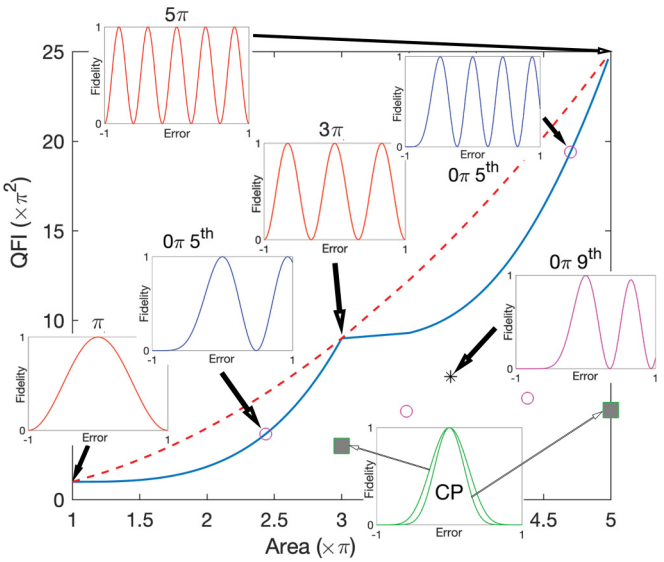

FIG. 5. Line of QFI reached by the QFI-NOP strategy (full line) (corresponding to the maximum QFI from Fig. 3) for each pulse area (from Fig. 4) when CPT is achieved, i.e., QFI = CFI. The bound of QFI [Eq. (8)] (dashed line) can be realized for $(2n+1)\pi$ pulses (when full and dashed lines intersect). The circles show four QFI's from fifth-order 0π-NOP; two are located on the QFI line. The asterisk indicates the QFI from ninth-order 0π-NOP. The green squares locate 3π and 5π CP QFIs, well below the optimal ones. The insets show typical forms of the CPT fidelity profiles as a function of the error α. One can identify the continuous modification of the profiles along the QFI line, from π- to 3π-pulse profiles passing by a fifth-order 0π-NOP profile (monotonic for $\alpha < 0$), and from 3π- to 5π-pulse profiles passing by the profile of another fifth-order 0π-NOP solution (but featuring a peak for $\alpha < 0$).

equations for the trajectory $(\gamma(t), \theta(t))$ that has to be minimized:

$$0 = \ddot{\gamma} + 2\dot{\gamma}\dot{\theta}\cot\theta + \frac{1}{2\sin\theta}\mu\dot{\theta}, \quad (24a)$$

$$0 = \ddot{\theta} - \dot{\gamma}^2\sin\theta\cos\theta - \frac{1}{2}\mu\dot{\gamma}\sin\theta, \quad (24b)$$

$$\dot{\mu} = \mu_1(\dot{\theta}\cos z - \dot{\gamma}\sin\theta\sin z) - \mu_2(\dot{\theta}\sin z + \dot{\gamma}\sin\theta\cos z), \quad (24c)$$

$$\dot{z} = \dot{\gamma}\cos\theta. \quad (24d)$$

From the first two equations, it follows that $\Omega = (\dot{\theta}^2 + \dot{\gamma}^2\sin^2\theta)^{1/2}$ is a constant of motion, meaning that the optimal narrowband pulse amplitude appears to be constant $\Omega(t) = \Omega_0 = |\dot{\theta}_i| > 0$. From Eq. (24a) at the initial time t_i, we obtain $\dot{\gamma}_i = -\mu(t_i)/4 \equiv -\mu_i/4$. In summary, the boundaries to be considered read:

$$\gamma_i = \frac{\pi}{2}, \quad \dot{\gamma}_i = -\frac{\mu_i}{4}, \quad \theta_i = 0, \quad \theta_f = \pi,$$
$$|\dot{\theta}_i| = \Omega_0, \quad z_i = 0. \quad (25)$$

We normalize with respect to Ω_0: $\mu_j = \tilde{\mu}_j\Omega_0$, $j = 1, 2$, $\mu = \tilde{\mu}\Omega_0$, and $t = \tilde{t}/\Omega_0$. From the solution of Eq. (24), one can find the shape of the detuning $\Delta(t)$ using Eq. (16a).

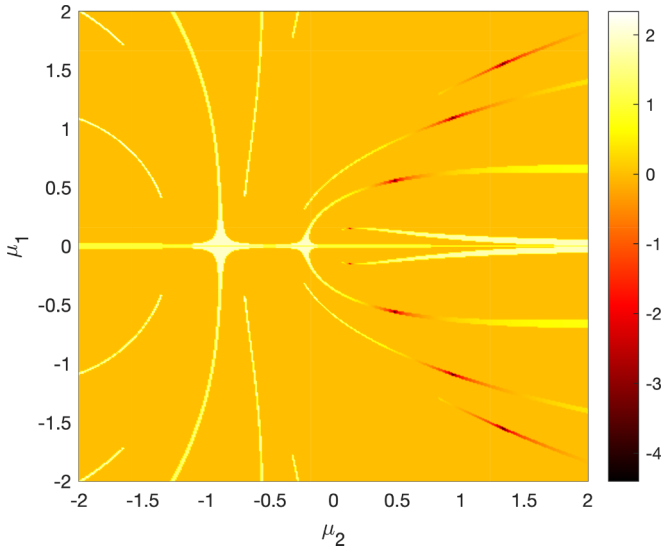

FIG. 6. Landscape as contour plot of $|Q_1|$ [Eq. (E5a)] when $\theta = \theta_f = \pi$ (in a logarithmic scale) as a function of the two (dimensionless) Lagrangian multipliers for $\mu_i = 0$ (optimal value). A series of four minimum values (as dark points) are exhibited for negative μ_1, corresponding to circles in Fig. 5, and symmetrically for positive μ_1 (leading to the same respective profiles).

Comparing it to Eq. (24a) and using the derivative of Eq. (5c), we can conclude that

$$\Delta = \tfrac{1}{2}\mu. \tag{26}$$

A similar procedure for the ninth-order 0π-NOP can be found in Appendix F.

We notice that this strategy has the technical advantage compared to the QFI-NOP that derivatives of higher orders can be addressed directly by nullifying each of them.

IV. OPTIMAL QUANTUM SENSING: NUMERICS

A. QFI-NOP

The landscape of the QFI from the differential equations (20) satisfying the boundaries (21) is plotted in Fig. 3. The corresponding pulse area is shown in Fig. 4. From these results, we deduce the maximum reachable QFI for each pulse area in Fig. 5 (full line). More specifically, for each pulse area (by fixing the final time T), we found the pairs (λ_1, λ_2) that satisfy the boundaries (21) and we retained the one corresponding to the maximum value of the QFI.

One recovers the limit of π-pulse transfer leading to the theoretical maximum value of QFI $= \mathcal{A} = \pi$ for such pulse area. Above the area π, the QFI increases first slowly and next sharply until the area 3π. We observe the same behavior from 3π to 5π. We observe that, except for the $(2n+1)\pi$-pulse transfer, where the maximum QFI is reached, the QFI is below the theoretical maximum value $\mathcal{A}^2$.

B. Fifth-order 0π-NOP

In Fig. 6, the landscape of $|Q_1|$ [Eq. (E5a)] from the differential equations (24) satisfying the boundaries (25) as a function of the two Lagrangian multipliers for $\mu_i = 0$ shows four minimum pairs for positive μ_1 and symmetrically for negative μ_1. These minimal values, which are numerically shown to go to zero only for $\mu_i = 0$, can be characterized more precisely by an optimization procedure that consists in finding the Lagrangian multiplier pairs (μ_1, μ_2) such that the solutions of equations (24) satisfy the boundaries [Eq. (25)] and the constraint $|Q_1| = 0$ [whatever $\gamma(t_f)$]. The final time $t_f = T$ is not fixed in the procedure. The four minima are positioned in Fig. 5 as circles. Two of them lie on the line of maximum QFI and can thus be identified as optimal.

The profile of the one associated with the smallest area ($\mathcal{A} \approx 2.435\pi$, $\mathcal{F}_Q \approx 3.67\pi^2$) presents the interesting feature of a monotonic behavior for $\alpha \leqslant 0$, as in the case of the CP but in a much more efficient way since it necessitates a 20% lower area than the 3π CP for a 20% larger QFI. However, contrary to the CP profile, the 0π-NOP profile is not symmetric around $\alpha = 0$ and is not flattened around $\alpha = 1$. Figure 5 shows that this 0π-NOP profile can be interpreted as the continuous modification from the π pulse to the 3π-pulse profiles along the maximum line of the QFI. For a pulse area above the one ($\mathcal{A} \approx 2.435\pi$) corresponding to this 0π-NOP, one can observe the emergence of a peak localized in $\alpha \in]-1, 0[$. This peak reaches CPT at the resonant 3π pulse.

The profile of the minimum associated with the largest area ($\mathcal{A} \approx 4.7\pi$, $\mathcal{F}_Q \approx 19.4\pi^2$) has a first peak in $\alpha \in]-1, 0[$ and can be interpreted as a continuous modification from the 3π-pulse to the 5π-pulse profiles. This pulse features a dramatic improvement of the QFI compared to the simple 3π pulse, from $9\pi^2$ to $19.4\pi^2$, with a qualitatively similar profile. For a pulse area above $\mathcal{A} \approx 4.7\pi$, one can observe a second peak emerging for $\alpha \in]-1, 0[$, which reaches CPT at the resonant 5π pulse.

Figure 7 displays the dynamics of $\gamma(t)$ and $\theta(t)$ of the 0π-NOP of area $\mathcal{A} \approx 2.435\pi$. We have found that γ is time-symmetric, while θ is antisymmetric:

$$\gamma(t) = \gamma(T - t), \tag{27a}$$

$$\theta(t) = \pi - \theta(T - t). \tag{27b}$$

The lower frame of Fig. 7 illustrates the symmetric trajectory θ as a function of γ.

Figure 8 displays the population dynamics from the ground state and the detuning resulting from the optimal trajectories $\theta(t)$ and $\gamma(t)$ of Fig. 7. This optimal detuning features a simple smooth form that can be easily produced experimentally. The population dynamics is comparable to the 3π pulse in terms of oscillations, except that the first oscillation does not reach complete transfer nor complete population return.

Figures 9 and 10 show the optimal trajectories and the resulting population dynamics and detuning, respectively, for the pulse area $\mathcal{A} \approx 4.7\pi$. One can notice that the detuning has a similar form as the previous one but with a narrower variation. Population dynamics share similarities with the one of the 5π pulse but with transient incomplete oscillations as in the previous case.

C. Ninth-order 0π-NOP

The NIO Lagrange equations at ninth order [Eq. (F6)] are determined in Appendix F. The numerical search of the

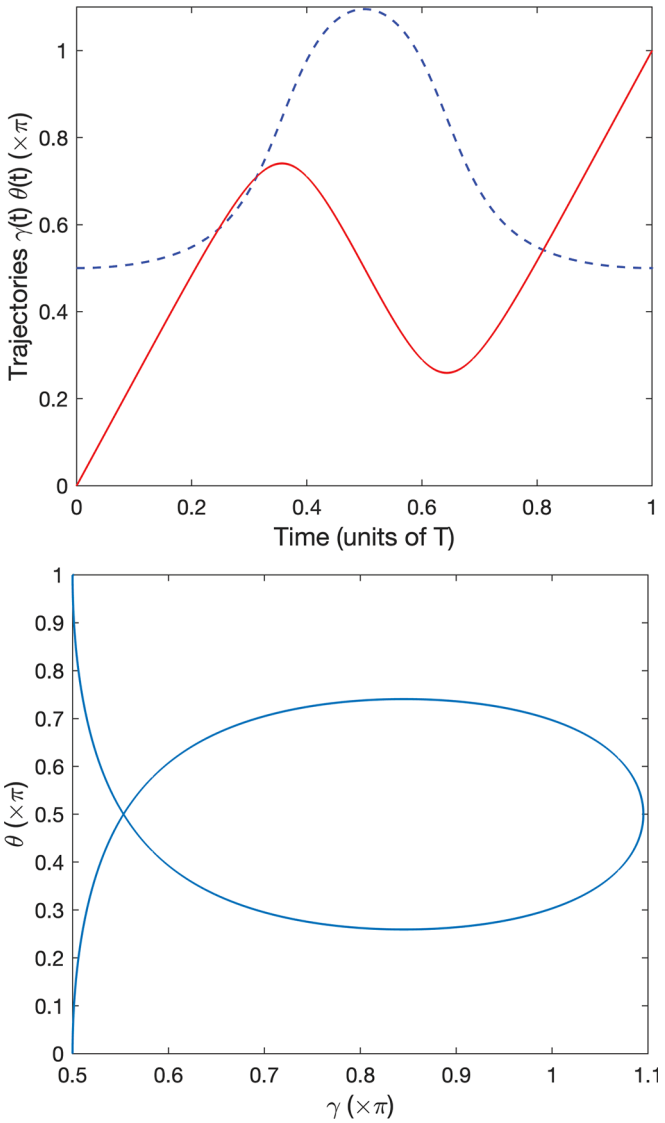

FIG. 7. Upper frame: Optimal trajectories $\theta(t)$ (full line), $\gamma(t)$ (dashed line) for fifth-order 0π-NOP with pulse area $\mathcal{A} \approx 2.435\pi$. Lower frame: corresponding optimal trajectory $\widetilde{\theta}(\gamma)$.

Lagrange multipliers and of the optimal time leading to CPT is difficult because (1) the unknown parameters (six including the optimal time) are numerous, which induces many local minima trapping the search procedure and (2) the dynamics near the target at the poles is unstable. We apply the following algorithm:

(1) We fix the final (large enough) optimal time of the process T and find the optimal Lagrangian multipliers satisfying the constraints $Q_1 = Q_3 = 0$ (at a certain precision), which leads to a certain target angle θ_f for this time T. We have to apply the search many times using random initial Lagrangian multipliers until finding the solution.

(2) We next slightly increase, $T' > T$, or decrease, $T' < T$, the final optimal time and launch the optimization algorithm starting with the previously found Lagrangian parameters as initial values. This results in a larger target angle $\theta'_f > \theta_f$.

(3) Iteratively, we modify the final time resulting in an increasing target angle until reaching $\theta_f = \pi$.

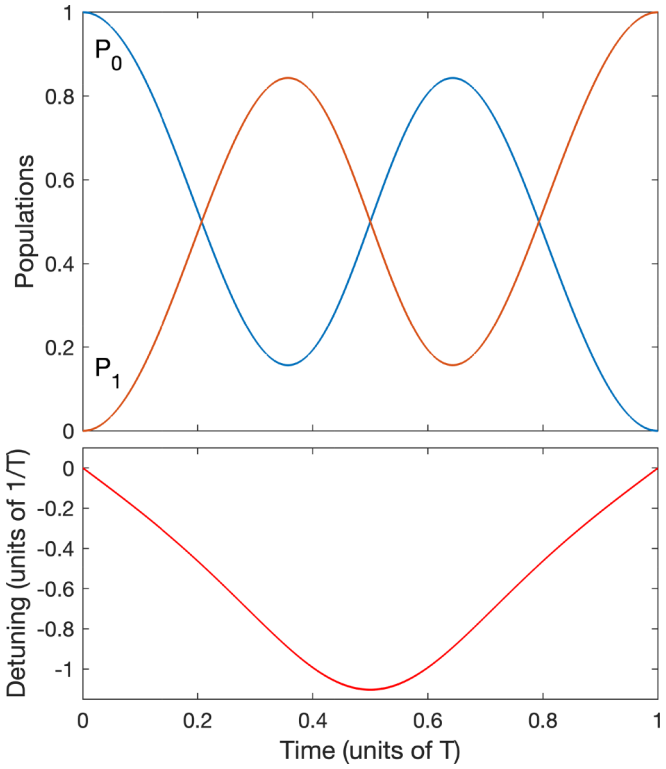

FIG. 8. Population dynamics $P_j = |\langle j|\phi_0(t)\rangle|^2$, $j = 0, 1$ (upper frame), associated with the detuning (lower frame) with the square pulse of amplitude $\Omega_0 \approx 2.435\pi/T$ resulting from the optimal trajectories $\theta(t)$ and $\gamma(t)$ of Fig. 7.

This algorithm assumes a continuous variation of the Lagrange multipliers as a function of θ_f. We found a solution for the ninth-order 0π-NOP for the parameters $\mu_3 \approx -0.04943$, $\mu_4 \approx 0.13557$, $\mu_{5,i} \approx -0.54684$, $\mu_{6,i} \approx -1.43772$, and $\mu_{7,i} \approx 1.01249$, featuring a semiglobal

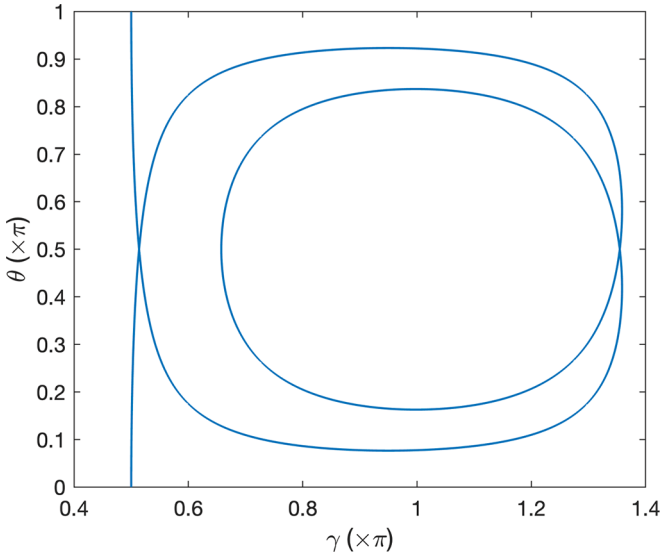

FIG. 9. Optimal trajectory $\widetilde{\theta}(\gamma)$ for fifth-order 0π-NOP with pulse area $\mathcal{A} \approx 4.7\pi$.

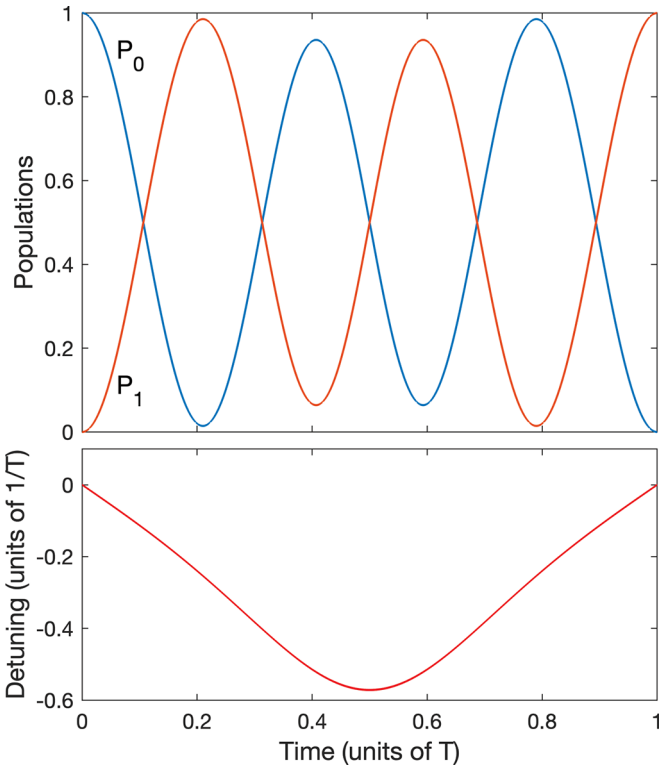

FIG. 10. Same as Fig. 8 but for the optimal trajectory of Fig. 9.

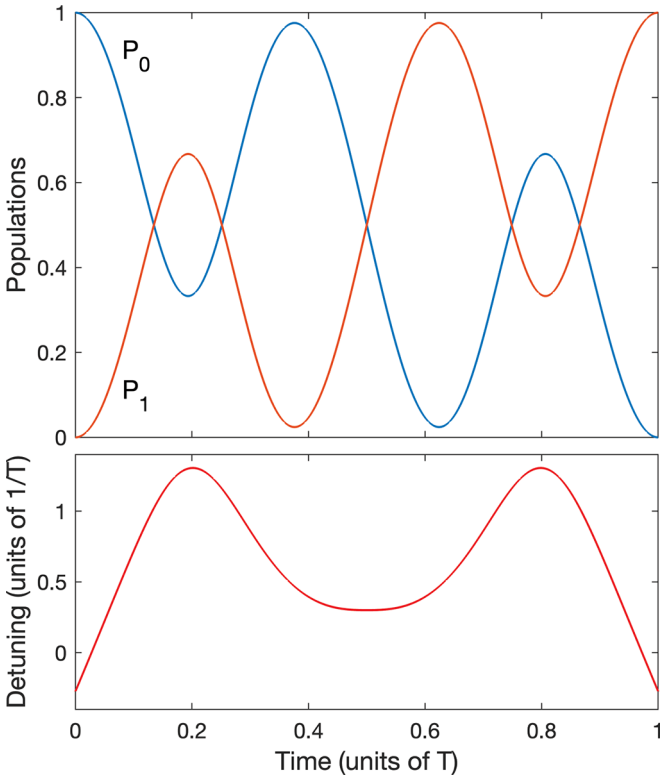

FIG. 12. Same as Fig. 8 but for the optimal trajectory of Fig. 11.

profile, i.e., monotonic for $\alpha < 0$ (see Fig. 2). The pulse area is only 3.81π, which, compared to the CP technique requiring a 5π-pulse sequence for the same order, represents a pulse-area reduction of 24%. Moreover, the QFI derived for the ninth-order 0π-NOP, $\mathcal{F}_{\rm Q} \approx 6.87\pi^2$, is 37% larger than the CP technique QFI, $\mathcal{F}_{{\rm Q},(2n+1){\rm CP}} = 5\pi^2$.

The trajectory of the optimal solution can be found in Fig. 11 with the same kind of symmetries [Eq. (27)]

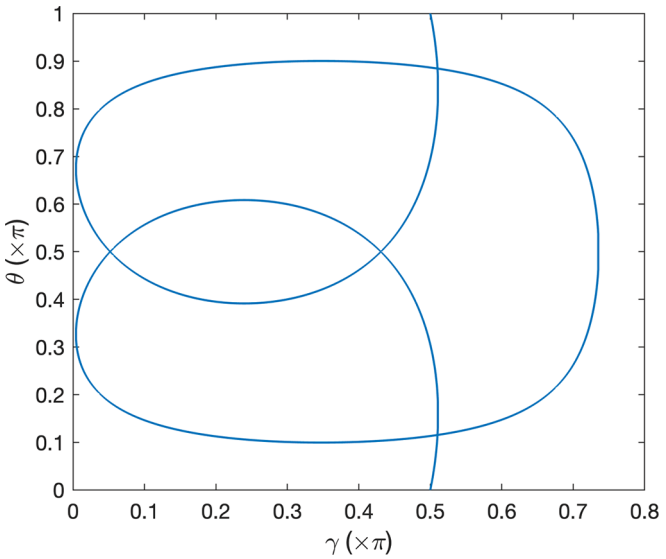

FIG. 11. Optimal trajectory $\widetilde{\theta}(\gamma)$ for ninth-order 0π-NOP with pulse area $\mathcal{A} \approx 3.81\pi$.

as before. Figure 12 shows the population dynamics and the detuning from the trajectory of Fig. 11: It is slightly more complex compared to the previous cases. The dynamics significantly deviates from the 3π- or 5π-pulse dynamics.

The comparative CPT profiles of π-pulse, fifth- and ninth-order 0π-NOP are displayed in Fig. 13. We observe the increasing QFI, i.e., a narrower profile at the peaks around $\alpha = 0$, for higher-order optimization associated with the flattening near $\alpha = -1$ and to larger pulse areas, as expected. We notice the nonsymmetric 0π-NOP curves around $\alpha = 0$ (except in the region very close to the peaks at $\alpha = 0$), contrary to CP profiles (see Figs. 1 and 2).

V. QUANTUM SENSING PROTOCOL: IMPLEMENTATION ON IBM'S QUANTUM COMPUTER

A. Implementation on IBM's quantum computer

IBM [38] provides open access to their quantum computers based on superconducting transmon qubits. With the use of the Python programming language and the Qiskit library [39], specifically Qiskit pulse [40], one is able to shape pulses online [47]. We recently proposed a digital shaping of the detuning overcoming the limitation of the sampling time for a direct discretization [44]. The digitization consists of using a train of short resonant subpulses to mimic a continuous detuning in sampling it via the (constant) phase of the subpulses:

$$\hat{H}(t) = \frac{1}{2}\hbar \sum_n \Omega_n \mathbf{1}_n(t) \Lambda\left(\frac{t - t_n}{\sigma}\right) \begin{bmatrix} 0 & e^{-i\varphi_n} \\ e^{i\varphi_n} & 0 \end{bmatrix}, \qquad (28)$$

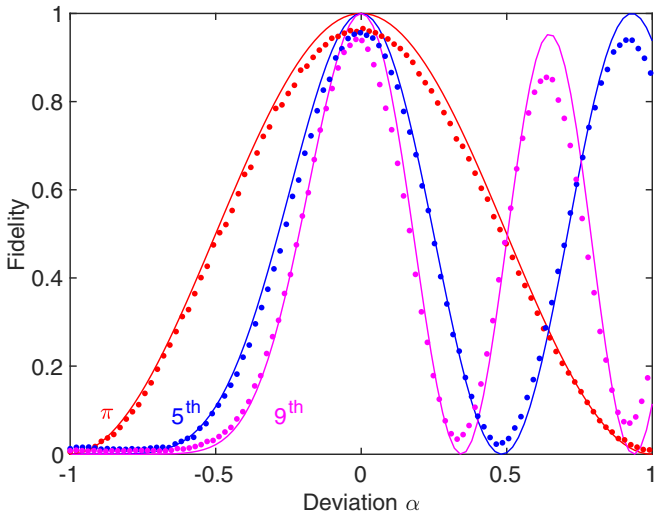

FIG. 13. Comparative CPT fidelity profiles (full line) of π-pulse, fifth- and ninth-order 0π-NOP, associated with the respective pulse areas: π, 2.435π, 3.81π, and the respective QFI: π^2, $3.67\pi^2$, $6.87\pi^2$, as functions of the deviation α, with their experimental demonstration on the IBMs "ibmq-lima" quantum computer (dotted lines). The errors between experiment and theory are mainly due to readout (around 4%).

where each subpulse of shape $\Lambda(t)$, amplitude Ω_n, phase φ_n, and characteristic duration σ is centered around $t_n = n\tau$, with τ the delay between two consecutive subpulses. In our case, we take Gaussian subpulses, $\Lambda(t) = e^{-t^2}$, with $\tau = 6\sigma$ such that we can neglect the indicator function $\mathbf{1}_n(t)$ ($\mathbf{1}_n(t) = 1$ when $t \in [t_{n-1/2}, t_{n+1/2}[$, otherwise it is 0) because the subpulses do not overlap with each other. It can be shown that to have accurate results we can take identical Gaussian subpulses with identical Ω_0 amplitudes (for a constant global pulse) and σ durations and only change the phase $\varphi_n = \varphi(t_n)$ between these subpulses in a way that mimics the continuous detuning $\Delta(t)$, from integration of

$$\Delta = \varphi' + \frac{\tau^2}{24}\varphi''' + \cdots = \varphi'[1 + O((\tau/T)^2)] \approx \varphi'. \quad (29)$$

The results for the phases from the fifth-order detuning of Fig. 10 and from the ninth-order detuning of Fig. 12 can be found in Fig. 14 and in Fig. 15, respectively.

In Fig. 13, we show the experimental implementation of the square Rabi π-pulse, fifth- and ninth-order 0π-NOP solutions on the IBM's "ibmq-lima" quantum computer compared to its respective theoretical profiles. In Fig. 13, the value of $\alpha = 0$ of the experimental data is calibrated at the first peak of the profiles. For each experiment, we have used a train of digitizing 21 Gaussian pulses, identical in their amplitude and duration $\sigma = 5 \times \sqrt{2}$ ns. For the Rabi process, we used a square pulse of duration τ. Each experiment was repeated 8096 times in order to get accurate average values for the fidelity. The errors are mainly due to readout, as mentioned in the guideline [38] and due to the sampling time $t_{\text{samp}} \approx 0.222$ ns. The experiment was conducted on qubit number 0 with a frequency of 5.03 GHz and anharmonicity -0.33574 GHz. We observe a very good agreement between the theoretical profiles and their experimental implementation.

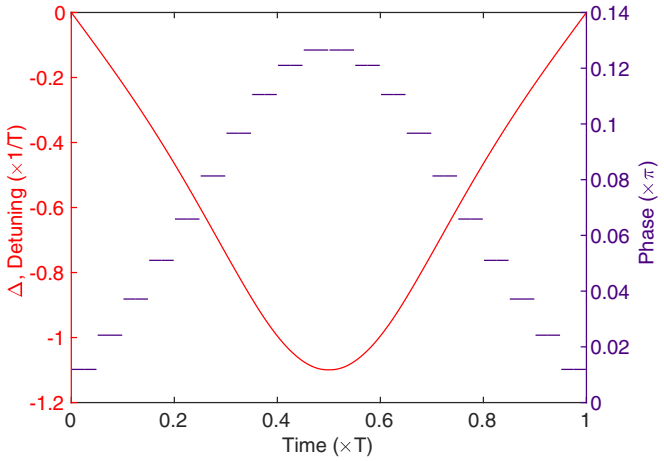

FIG. 14. Detuning as a function of time of fifth-order 0π-NOP (full line) of Fig. 10 and the corresponding (piecewise) phases of each subpulse for a train of 21 digitizing subpulses.

B. Parameter determination on IBM's quantum computer: Protocol and results

The determination of the parameter α and its precision are based on the theoretical CPT fidelity profile (see Figs. 1 and 2), denoted $\mathsf{F}_{\text{theo.}}(\alpha)$, where $\alpha = 0$ is a first estimation of the exact value, of the asymptotic form

$$\mathsf{F}_{\text{theo.}}(\alpha) \sim 1 - \tfrac{1}{4}\alpha^2\mathcal{F}_{\text{Q}} \quad (30)$$

in the vicinity of $\alpha = 0$.

One can thus determine an estimate of the (exact) experimental value α_e from the measurement of the CPT fidelity using the theoretical CPT fidelity profile, $\mathsf{F}_{\text{theo.}}(\alpha_e) \sim 1 - \frac{1}{4}\alpha_e^2\mathcal{F}_{\text{Q}}$. This principle holds for α_e close enough to $\alpha = 0$, i.e., in the quadratic region of the profile [Eq. (30)]. From the determination of α_e, we obtain Ω in the units of the experiment via the relation $\Omega_e = \Omega(1 + \alpha_e)$. In practice, we will determine the estimate of α_e as well as a confidence interval $\alpha_e \in [\alpha_1, \alpha_2]$, which we will make as small as possible using a narrow profile. The confidence interval is deduced from the measured mean value of the fidelity $\pm$ the standard deviation

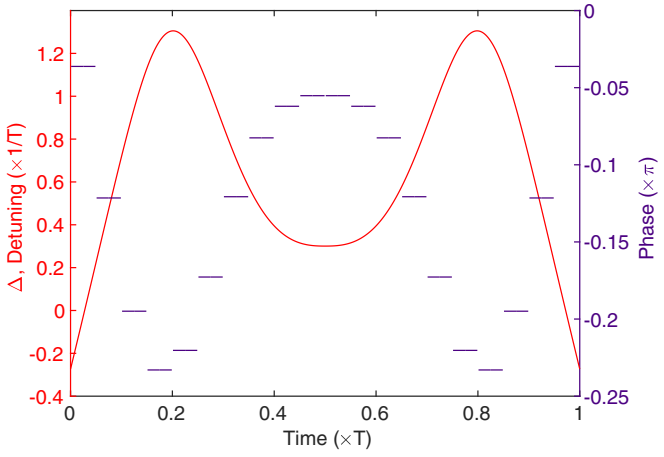

FIG. 15. Same as Fig. 14 but for ninth-order 0π-NOP of Fig. 12.

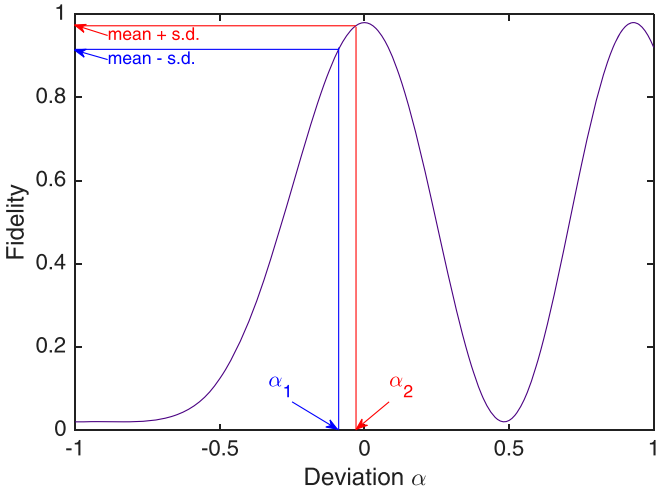

FIG. 16. From a given theoretical profile [Eq. (30)], plot of the interval of the population measurements in the excited state bounded by the mean value ± the standard deviation (s.d.), associated with an α segment $[\alpha_1, \alpha_2]$. A given interval of the fidelity profile corresponds to a smaller α segment for a larger QFI, hence to a better precision of α. Note that, according to Fig. 13, we have artificially introduced an error in the profile mimicking the readout error.

of the mean (see Fig. 16). Our goal is to demonstrate that one can get a better accuracy for a narrower profile.

In the experiment, the mean value and standard deviation are determined for each fidelity from 1000 trials. A first estimation of α has been derived by constructing a Rabi cycle with a square pulse of varying area via Ω_0 for a fixed time of interaction, and taking the peak value (π pulse). To operate on a given side of the profile (here negative α is chosen), we have used a pulse $\Omega_e = 0.9\Omega_0$ in all experiments. The results in α for different points along the line of maximum QFI (see Fig. 5) are presented in Table I.

At the time of the experiment, we used the "ibm-osaka" quantum machine's first qubit. We observe that increasing the pulse area, and therefore the QFI, results in a narrower range, indicating a more precise estimation. According to the result from the largest QFI, the mean value of α_e is around $\alpha_{\text{mean}} = -8.4\%$ in the interval $[\alpha_1 = -8.2\%, \alpha_2 = -8.6\%]$.

TABLE I. The parameters α_1 and α_2 (in absolute values) are found according to the method shown in Fig. 16; α_{mean} is the value of α for which the fidelity is equal to the mean fidelity of the IBM experiment (see text). The table shows that by increasing the pulse area and the QFI, the range of the deviation decreases resulting in a more precise parameter estimation.

Area	QFI $\mathcal{F}_Q$	$\lvert\alpha_2\rvert$	$\lvert\alpha_1\rvert$	$\lvert\alpha_2 - \alpha_1\rvert$	$\lvert\alpha_{\text{mean}}\rvert$
2.435π	36.2	5.5%	7.3%	1.8%	6.5%
2.8π	65.3	6.8%	7.8%	1%	7.3%
2.9π	76.3	8%	8.7%	0.7%	8.4%
3π	88.8	8.2%	9.0%	0.8%	8.6%
3.6π	93.9	7.7%	8.5%	0.8%	8.1%
4.6π	175.9	8.3%	8.7%	0.4%	8.5%
4.9π	224.1	8.2%	8.6%	0.4%	8.4%

This shows that the relative accuracy has been improved by a factor of five between the estimation from the lowest QFI ($\mathcal{F}_Q = 36.2$) and from the largest QFI we have considered ($\mathcal{F}_Q = 224$), and of more than one order of magnitude compared to the simple π pulse. The improvement of the accuracy (i.e., the reduction of $|\alpha_1 - \alpha_2|$) approximately follows the inverse of the increase of the QFI, as can be deduced from the calculation:

$$\mathsf{F}_{\text{theo.}}(\alpha_2) - \mathsf{F}_{\text{theo.}}(\alpha_1) \sim \tfrac{1}{2}\mathcal{F}_Q(\alpha_1 - \alpha_2)\alpha_{\text{mean}}, \tag{31}$$

i.e.,

$$\alpha_1 - \alpha_2 \sim 2\frac{\mathsf{F}_{\text{theo.}}(\alpha_2) - \mathsf{F}_{\text{theo.}}(\alpha_1)}{\alpha_{\text{mean}}}\frac{1}{\mathcal{F}_Q}, \tag{32}$$

where the mean value α_{mean}, determined as $\alpha_{\text{mean}} \sim (\alpha_1 + \alpha_2)/2$, and $\mathsf{F}_{\text{theo.}}(\alpha_2) - \mathsf{F}_{\text{theo.}}(\alpha_1)$ weakly depend on the QFI $\mathcal{F}_Q$ (determined at $\alpha = 0$). We anticipate an improvement of several orders of magnitude for a pulse with a large (odd) number of π.

VI. CONCLUSION

We have proposed a narrowband optimal control strategy for quantum sensing of the Rabi frequency coupling in the situation where QFI equals CFI, meaning that one targets CPT. This features the practical advantage of being relatively easy to measure because it does not involve phases and complex tomographic methods. We have introduced two distinct approaches: the QFI-NOP and 0π-NOP. The QFI-NOP method is designed to maximize the QFI around $\alpha = 0$, which corresponds to a first estimation of the Rabi frequency, with optimal pulses. In this approach, we have shown that the resulting QFIs are remarkably close to their maximum bounds. In particular, resonant pulses with areas that are odd multiples of π achieve the maximum bounds. However, QFI-NOP pulses generally produce an oscillatory profile that is only locally narrow. This may be less practical when the Rabi frequency is entirely unknown, as identifying the correct peak among multiple peaks becomes difficult. A first estimate from a π pulse is necessary to correctly apply this approach.

On the other hand, the 0π-NOP approach is designed to flatten the profile near $\alpha = -1$ (corresponding to a 0π pulse). We have shown that it can provide a semiglobal profile, i.e., which is monotonic for $\alpha \leqslant 0$. We find that the fifth-order 0π-NOP pulse is in fact one of the QFI-NOP pulses, since the resulting QFI is located on the QFI line in Fig. 5. However, this is not true for the ninth-order 0π-NOP pulse.

The optimal semiglobal profile may find an important application for the *optimal selective excitation* of an atom or ion to be locally addressed within a chain, as, e.g., in an ion trap platform [48], or in a two-dimensional optical lattice [49], as originally proposed with the use of CP [50]. Associating the Gaussian intensity profile of the laser beam to the α variable, we can identify the values $\alpha = -1$ to no intensity and 0 to its maximum at the beam center. The transfer profile of the 0π-NOP pulse then results in a *global narrowband spatial transfer profile*.

The optimal manipulation of the profile as broadband (RIO) or narrowband (NIO) opens further perspectives such as optimal passband pulses [51]. We note that optimal nar-

rowband pulses as a function of detuning can be generated by the method presented in this paper.

ACKNOWLEDGMENTS

D.S. and B.P. gratefully acknowledge useful discussions with D. Guéry-Odelin and N. Ombredane. We thank the support from the Erasmus Mundus Master QuanTEEM (Project No. 101050730), the project QuanTEdu-France (Grant No. ANR-22-CMAS-0001) on quantum technologies, the EUR-EIPHI Graduate School (Grant No. 17-EURE-0002), the ANR project QuCoBEC (Grant No. ANR-22-CE47-0008-02), and Région Bourgogne-Franche-Comté and Dijon Métropole.

DATA AVAILABILITY

The data supporting this study's findings are available within the article.

APPENDIX A: QUANTUM FISHER INFORMATION

In this Appendix, we recall the basic definitions of the quantum and the classical Fisher informations. We consider a quantum system defined in a Hilbert space $\mathcal{H}$ whose dynamics are governed by the Hamiltonian $\hat{H}_X$ that depends on an unknown parameter X. The time evolution of the quantum state $|\psi_X\rangle$ also depends on the parameter X. We can therefore define a distance, at a nonzero time t_f, between two states $|\psi_{X_1}(t_f)\rangle$ and $|\psi_{X_2}(t_f)\rangle$, for the same initial condition $|\psi_i\rangle$. A natural way to define this distance is to use the Fubiny-Study metric that leads to

$$d^2(|\psi_{X_1}\rangle, |\psi_{X_2}\rangle) = \text{acos}^2(\sqrt{\langle\psi_{X_2}|\psi_{X_1}\rangle\langle\psi_{X_1}|\psi_{X_2}\rangle}), \tag{A1}$$

where d denotes the distance between the two states. For two sufficiently close values X_1 and X_2 of X, the corresponding states $|\psi_{X_1}(t_f)\rangle$ and $|\psi_{X_2}(t_f)\rangle$ are very close so that the distance [Eq. (A1)] can be approximated by a first-order expansion as follows:

$$d^2(|\psi_{X_1}\rangle, |\psi_{X_2}\rangle) = 1 - |\langle\psi_{X_1}|\psi_{X_2}\rangle|^2. \tag{A2}$$

Equation (A2) highlights a general strategy used in the estimation of quantum parameters, which consists of maximizing at a time t_f the distance between the two states $|\psi_{X_1}\rangle$ and $|\psi_{X_2}\rangle$ in order to find the value of the unknown parameter by a measurement of the quantum state. A more precise and local statement of this idea can be derived as follows. We set $|\psi_{X_1}\rangle = |\psi_{X_0}\rangle$ and $|\psi_{X_2}\rangle = |\psi_{X_0+dX}\rangle$, where dX is a small variation around $X = X_0$, with X_0 being a preliminary estimate of the unknown parameter. The corresponding state can be written at first order as

$$|\psi_{X_0+dX}\rangle = |\psi_{X_0}\rangle + |\partial_X\psi_{X_0}\rangle dX + O(dX^2), \tag{A3}$$

where we denote $|\partial_X\psi_{X_0}\rangle = \frac{\partial|\psi_{X_0}\rangle}{\partial X}$. Using Eq. (A2), the distance d between $|\psi_{X_0}\rangle$ and $|\psi_{X_0+dX}\rangle$ is given by

$$d^2 = 1 - |\langle\psi_{X_0+dX}|\psi_{X_0}\rangle|^2.$$

From Eq. (A3), we deduce up to the terms of order two that

$$|\langle\psi_{X_0+dX}|\psi_{X_0}\rangle|^2 = 1 + dX\langle\psi_{X_0}|\partial_X\psi_{X_0}\rangle + dX\langle\partial_X\psi_{X_0}|\psi_{X_0}\rangle + dX^2|\langle\partial_X\psi_{X_0}|\psi_{X_0}\rangle|^2.$$

From $\langle\psi_{X_0+dX}|\psi_{X_0+dX}\rangle = 1$, we obtain the relation

$$dX\langle\psi_{X_0}|\partial_X\psi_{X_0}\rangle + dX\langle\partial_X\psi_{X_0}|\psi_{X_0}\rangle = -dX^2\langle\partial_X\psi_{X_0}|\partial_X\psi_{X_0}\rangle,$$

which leads to

$$d^2 = dX^2\langle\partial_X\psi_{X_0}|\partial_X\psi_{X_0}\rangle - dX^2|\langle\partial_X\psi_{X_0}|\psi_{X_0}\rangle|^2.$$

The QFI, denoted as $\mathcal{F}_\text{Q}$, is finally defined from the local curvature of the square distance around the estimate X_0 of the parameter, as

$$\mathcal{F}_\text{Q} = 4[\langle\partial_X\psi_{X_0}|\partial_X\psi_{X_0}\rangle - |\langle\partial_X\psi_{X_0}|\psi_{X_0}\rangle|^2]. \tag{A4}$$

The local character of the QFI can be clearly seen in Eq. (A4) since it depends only on the state and its derivative in X_0.

We now derive two other expressions for the QFI that will be useful in the context of its maximization. In order to simplify the expressions, we omit below the index X_0 in the state and in the Hamiltonian. The dynamics of the states $|\psi(t)\rangle$ and $\partial_X|\psi(t)\rangle$ are given by the Schrödinger equation and its derivative with respect to X as

$$\imath\frac{d}{dt}\begin{pmatrix}|\psi(t)\rangle\\ |\partial_X\psi(t)\rangle\end{pmatrix} = \begin{pmatrix}\hat{H}(t) & 0\\ \partial_X\hat{H}(t) & \hat{H}(t)\end{pmatrix}\begin{pmatrix}|\psi(t)\rangle\\ |\partial_X\psi(t)\rangle\end{pmatrix}, \tag{A5}$$

with the initial conditions $|\psi(t_i)\rangle = |\psi_i\rangle$ and $|\partial_X\psi_i\rangle = 0$ and with units such that $\hbar = 1$. The formal solution of this system can be expressed as

$$\begin{pmatrix}|\psi(t)\rangle\\ |\partial_X\psi(t)\rangle\end{pmatrix} = \begin{pmatrix}\hat{U}(t) & 0\\ \partial_X\hat{U}(t) & 0\end{pmatrix}\begin{pmatrix}|\psi_i\rangle\\ 0\end{pmatrix}, \tag{A6}$$

where

$$\hat{U}(t) = \mathbb{1} - \imath\int_{t_i}^{t}\hat{H}(\tau)\hat{U}(\tau)d\tau$$

and

$$\partial_X\hat{U}(t) = -\imath\hat{U}(t)\int_{t_i}^{t}\hat{U}^\dagger(\tau)\partial_X\hat{H}(\tau)\hat{U}(\tau)d\tau. \tag{A7}$$

For the QFI, we arrive at

$$\begin{aligned}\mathcal{F}_\text{Q}(t) &= 4(\langle\partial_X\psi(t)|\partial_X\psi(t)\rangle - |\langle\psi(t)|\partial_X\psi(t)\rangle|^2)\\ &= 4(\langle\psi_i|\partial_X\hat{U}^\dagger(t)\partial_X\hat{U}(t)|\psi_i\rangle\\ &\quad - |\langle\psi_i|\hat{U}^\dagger(t)\partial_X\hat{U}(t)|\psi_i\rangle|^2).\end{aligned}$$

Introducing the operator $\hat{A}(t) = \int_{t_i}^{t}\hat{U}^\dagger(\tau)\partial_X\hat{H}(\tau)\hat{U}(\tau)d\tau$, we obtain

$$\mathcal{F}_\text{Q}(t) = 4(\langle\psi_i|\hat{A}^2(t)|\psi_i\rangle - |\langle\psi_i|\hat{A}(t)|\psi_i\rangle|^2).$$

Finally, the QFI is equal to four times the variance of the operator $\hat{A}(t)$,

$$\mathcal{F}_\text{Q}(t) = 4(\langle\hat{A}^2(t)\rangle_{|\psi_i\rangle} - \langle\hat{A}(t)\rangle^2_{|\psi_i\rangle}) = 4\text{Var}[\hat{A}(t)]_{|\psi_i\rangle}, \tag{A8}$$

which depends on the initial condition $|\psi_i\rangle$. Equation (A8) can be expressed as a function of the state $|\psi(t)\rangle$ at time t by using

the relation $|\psi_i\rangle = \hat{U}^\dagger(t)|\psi(t)\rangle$:

$$\mathcal{F}_Q(t) = 4\mathrm{Var}[\hat{A}'(t)]_{|\psi(t)\rangle}, \tag{A9}$$

where $\hat{A}'(t) = \hat{U}(t)\int_{t_i}^{t}\hat{U}^\dagger(\tau)\partial_X\hat{H}(\tau)\hat{U}(\tau)d\tau\hat{U}^\dagger(t)$.

Another expression of the QFI can be derived as follows. From the definition of the operator $\hat{A}(t)$, we have

$$\langle\hat{A}(t)\rangle = \int_{t_i}^{t}\langle\psi(\tau_1)|\partial_X\hat{H}(\tau_1)|\psi(\tau_1)\rangle d\tau_1$$

and

$$\langle\hat{A}^2(t)\rangle = \int_{t_i}^{t}\int_{t_i}^{t}\langle\psi(\tau_1)|\partial_X\hat{H}(\tau_1)\hat{U}(\tau_1) \times\hat{U}^\dagger(\tau_2)\partial_X\hat{H}(\tau_2)|\psi(\tau_2)\rangle d\tau_2 d\tau_1.$$

Introducing the basis $\{|\Phi_k\rangle \in \mathcal{H},\ k = 1,\ldots,\dim(\mathcal{H})-1\}$ of the subspace orthogonal to $|\psi_i\rangle$ and the closure relation

$$|\psi_i\rangle\langle\psi_i| + \sum_{k=1}^{\dim(\mathcal{H})-1}|\Phi_k\rangle\langle\Phi_k| = \mathbb{1},$$

we obtain

$$\hat{U}(\tau_1)\mathbb{1}\hat{U}^\dagger(\tau_2) = |\psi(\tau_1)\rangle\langle\psi(\tau_2)| + \sum_{k=1}^{\dim(\mathcal{H})-1}|\Phi_k(\tau_1)\rangle\langle\Phi_k(\tau_2)|,$$

and we arrive at

$$\begin{aligned}\langle\hat{A}^2(t)\rangle = &\int_{t_i}^{t}\int_{t_i}^{t}\langle\psi(\tau_1)|\partial_X\hat{H}(\tau_1)|\psi(\tau_1)\rangle \\ &\times\langle\psi(\tau_2)|\partial_X\hat{H}(\tau_2)|\psi(\tau_2)\rangle d\tau_2 d\tau_1 \\ &+\sum_{k=1}^{\dim(\mathcal{H})-1}\int_{t_i}^{t}\int_{t_i}^{t}\langle\psi(\tau_1)|\partial_X\hat{H}(\tau_1)|\Phi_k(\tau_1)\rangle \\ &\times\langle\Phi_k(\tau_2)|\frac{\partial\hat{H}(\tau_2)}{\partial X}|\psi(\tau_2)\rangle d\tau_2 d\tau_1.\end{aligned}$$

Finally, this yields

$$\begin{aligned}\langle\hat{A}^2(t)\rangle = &\left(\int_{t_i}^{t}\langle\psi(\tau_1)|\partial_X\hat{H}(\tau_1)|\psi(\tau_1)\rangle d\tau_1\right)^2 \\ &+\sum_{k=1}^{\dim(\mathcal{H})-1}\left|\int_{t_i}^{t}\langle\psi(\tau_1)|\partial_X\hat{H}(\tau_1)|\Phi_k(\tau_1)\rangle d\tau_1\right|^2.\end{aligned}$$

Plugging the expressions of $\langle\hat{A}^2(t)\rangle$ and $\langle\hat{A}(t)\rangle$ into Eq. (A8), we obtain the third expression of the QFI:

$$\mathcal{F}_Q(t) = 4\sum_{k=1}^{\dim(\mathcal{H})-1}\left|\int_{t_i}^{t}\langle\psi(\tau)|\partial_X\hat{H}(\tau)|\Phi_k(\tau)\rangle d\tau\right|^2. \tag{A10}$$

APPENDIX B: CLASSICAL FISHER INFORMATION

Denoting by $|\partial\phi\rangle$ the difference at first order in α between $|\phi_{\alpha+d\alpha}\rangle$ and $|\phi_\alpha\rangle$:

$$|\phi_{\alpha+d\alpha}\rangle = |\phi_\alpha\rangle + |\partial\phi\rangle d\alpha, \tag{B1}$$

we deduce that the CFI is given by

$$\mathcal{F}_C = 4\sum_{k=0}^{1}\frac{[\mathrm{Re}\,(\langle\partial\phi|k\rangle\langle k|\phi_\alpha\rangle)]^2}{|\langle k|\phi_\alpha\rangle|^2}. \tag{B2}$$

Since $\langle\phi_{\alpha+d\alpha}|\phi_{\alpha+d\alpha}\rangle = 1$, we get $\langle\phi_\alpha|\partial\phi\rangle + \langle\partial\phi|\phi_\alpha\rangle = 0$. Hence, $|\partial\phi\rangle$ can be expanded on the basis $\{|\phi_\alpha\rangle, |\phi_{\alpha,\perp}\rangle\}$ as

$$|\partial\phi\rangle = ib|\phi_\alpha\rangle + c|\phi_{\alpha,\perp}\rangle, \quad b\in\mathbb{R}, \quad c\in\mathbb{C}, \quad c = |c|e^{i\varphi_c}. \tag{B3}$$

Using Eq. (B1), and from the expressions of $|\phi_\alpha\rangle$ and $|\phi_{\alpha,\perp}\rangle$ (4), we arrive at

$$\mathcal{F}_C = 4|c|^2\cos^2(\varphi_c+\gamma). \tag{B4}$$

From the definition of the QFI [Eq. (1)], we also deduce that

$$\mathcal{F}_Q = 4(\langle\partial\phi|\partial\phi\rangle - |\langle\partial\phi|\phi_\alpha\rangle|^2) = 4|c|^2, \tag{B5}$$

which shows, as expected, that $\mathcal{F}_C \leqslant \mathcal{F}_Q$ for the PVM $\{|0\rangle\langle 0|, |1\rangle\langle 1|\}$. CFI reaches its bound, $\mathcal{F}_C = \mathcal{F}_Q$, when the phases satisfy $\varphi_c + \gamma = 0(\pi)$ according to Eq. (B4).

In terms of state, we establish the property:

If $|\phi_0\rangle = |0\rangle$ or $|1\rangle$, then $\mathcal{F}_C = \mathcal{F}_Q$ in the limit of small α.

The proof goes as follows. We denote by p_1 and p_0 the projections onto the states $|1\rangle$ and $|0\rangle$: $p_k = |\langle k|\phi_0\rangle|^2$. The CFI [Eq. (11)] can be expressed as

$$\mathcal{F}_C = \frac{1}{p_0}\left(\frac{dp_0}{d\alpha}\right)^2 + \frac{1}{p_1}\left(\frac{dp_1}{d\alpha}\right)^2. \tag{B6}$$

Using $p_0 + p_1 = 1$, we get

$$\mathcal{F}_C = \frac{1}{p_1(1-p_1)}\left(\frac{dp_1}{d\alpha}\right)^2. \tag{B7}$$

Using the relation (7) up to the second order, $p_1 = 1 - \frac{\alpha^2}{4}\mathcal{F}_Q$, we arrive (in the limit $\alpha \ll 1$) at

$$\mathcal{F}_C = \mathcal{F}_Q(1 + O(\alpha^2)). \tag{B8}$$

APPENDIX C: THE PERTURBATIVE EXPANSION IN THE SINGLE-SHOT-SHAPED PULSE METHOD

Following the decomposition of the Hamiltonian (3), which can be written in general $H_\alpha = H_0 + \alpha V_\alpha$, the perturbative propagator reads

$$\begin{aligned}U(t,t_i) &= U_0(t,t_i)\left[\mathbb{1} + \frac{\alpha}{i}W_1 + \left(\frac{\alpha}{i}\right)^2 W_2 + \cdots\right] \\ &= U_0(t,t_i)\begin{bmatrix}1+O_1+O_2+\cdots & Q_1+Q_2+\cdots \\ -(\bar{Q}_1+\bar{Q}_2+\cdots) & 1+\bar{O}_1+\bar{O}_2+\cdots\end{bmatrix},\end{aligned} \tag{C1}$$

where the propagator $U_0(t,t_i)$ associated with the unperturbed Hamiltonian $H_0(t)$ takes the general SU(2) form: $U_0(t,t_i) = \begin{bmatrix}a & -\bar{b}\\ b & \bar{a}\end{bmatrix}$ with $|a|^2+|b|^2 = 1$, and the perturbative matrix terms read

$$\alpha^n W_n = \int_{t_i}^{t}dt_0\,V_I(t_0)\int_{t_i}^{t_0}dt_1\,V_I(t_1)\cdots\int_{t_i}^{t_{n-2}}dt_{n-1}\,V_I(t_{n-1}). \tag{C2}$$

The perturbation in the interaction representation is defined as

$$V_I(t) = U_0^\dagger(t,t_i)V_\alpha(t)U_0(t,t_i) \tag{C3}$$

and leads to the matrix elements (at time t)

$$O_n = \left(\frac{\alpha}{i}\right)^n\langle 0|W_n|0\rangle, \quad Q_n = \left(\frac{\alpha}{i}\right)^n\langle 1|W_n|0\rangle. \tag{C4}$$

From the unitarity property of propagators, it follows that $|1 + O_1 + O_2 + \cdots|^2 + |Q_1 + Q_2 + \cdots|^2 = 1$, and, from Eq. (18) with the initial condition $\theta_i = 0$, the fidelity is of the form

$$\begin{aligned}\mathsf{F}(t) &:= |\langle\phi_0(t)|\phi_\alpha(t)\rangle|^2 = 1 - |Q_1 + Q_2 + \cdots|^2 \\ &\equiv 1 + \widetilde{O}_1 + \widetilde{O}_2 + \widetilde{O}_3 + \cdots, \end{aligned} \tag{C5}$$

where one can identify order by order each correction to the population transfer $\widetilde{O}_n \equiv \widetilde{O}_n(O(\alpha^n))$ as a function of the off-diagonal terms of the perturbative matrix of Eq. (C1), $n \geqslant 1$:

$$\widetilde{O}_1 = 0, \tag{C6a}$$

$$\widetilde{O}_{2n} = -|Q_n|^2 - 2\sum_{m=1}^{n-1} \mathrm{Re}\,(Q_{2n-m}\bar{Q}_m), \tag{C6b}$$

$$= -|Q_n|^2 \text{ when } \widetilde{O}_{2(1\leqslant m<n)} = 0. \tag{C6c}$$

$$\widetilde{O}_{2n+1} = -2\sum_{m=1}^{n} \mathrm{Re}\,(Q_{2n+1-m}\bar{Q}_m), \tag{C6d}$$

$$= 0 \text{ when } \widetilde{O}_{2(1\leqslant m\leqslant n)} = 0. \tag{C6e}$$

APPENDIX D: EULER-LAGRANGE EQUATIONS FOR QFI-NOP

The perturbation in the interaction representation [Eq. (C3)] reads

$$V_I(t) = U_0^\dagger(t,t_i)V_\alpha(t)U_0(t,t_i) = \hbar\begin{bmatrix} e(t) & f(t) \\ \bar{f}(t) & -e(t) \end{bmatrix}, \tag{D1}$$

with the functions

$$e(t) = \tfrac{1}{2}\alpha\Omega\cos\varphi\sin\theta, \tag{D2a}$$

$$f(t) = \tfrac{1}{2}\alpha(\dot{\gamma}\sin\theta\cos\theta - i\dot{\theta})e^{i\gamma}. \tag{D2b}$$

The first-order curvature (C6a) of the excitation profile (19) is null. The second-order curvature (C6b) can be written as

$$\begin{aligned}\widetilde{O}_2(t) &= -\frac{1}{4}\alpha^2\left|\int_{t_i}^{t}\left(\frac{1}{2}\dot{\gamma}\sin(2\theta) - i\dot{\theta}\right)e^{i\gamma}dt\right|^2 \\ &= -\frac{1}{4}\alpha^2\mathcal{F}_\mathrm{Q}(t). \end{aligned} \tag{D3}$$

This remarkably shows the connection of the QFI to the second-order curvature of the profile, as announced in Eq. (7):

$$\frac{d^2\mathsf{F}(t)}{d\alpha^2}(\alpha = 0) = -\frac{1}{2}\mathcal{F}_\mathrm{Q}(t) + O(\alpha). \tag{D4}$$

For the case of CPT at time t_f from the ground state, associated with the boundaries $\theta_i = 0$ and $\theta_f = \pi$, we obtain

$$\begin{aligned}\widetilde{O}_2(t) &= -\frac{1}{4}\alpha^2\left|\frac{1}{2}[e^{i\gamma}\sin(2\theta)]_{t_i}^{t_f} + 2\int_{t_i}^{t_f}\dot{\theta}e^{i\gamma}\sin^2\theta dt\right|^2 \\ &= -\alpha^2\left|\int_{t_i}^{t_f}(\psi_1 + i\psi_2)dt\right|^2 \end{aligned} \tag{D5}$$

with the respective real and imaginary parts

$$\psi_1 = \dot{\theta}\cos\gamma\sin^2\theta, \quad \psi_2 = \dot{\theta}\sin\gamma\sin^2\theta, \tag{D6}$$

and one can identify the QFI (at time t_f)

$$\mathcal{F}_\mathrm{Q} = 4(|\Psi_1|^2 + |\Psi_2|^2), \quad \Psi_j(\gamma,\theta) = \int_{t_i}^{t_f}\psi_j dt. \tag{D7}$$

The optimization can be applied with respect to a given cost, the pulse energy $\mathcal{E}$, area $\mathcal{A}$, or duration $T = t_f - t_i$, respectively:

$$\mathcal{E}(\gamma,\theta) = \int_{t_i}^{t_f} dt(\dot{\theta}^2 + \dot{\gamma}^2\sin^2\theta) = \int_{t_i}^{t_f} dt\ \Omega^2, \tag{D8a}$$

$$\mathcal{A}(\gamma,\theta) = \int_{t_i}^{t_f} dt\sqrt{\dot{\theta}^2 + \dot{\gamma}^2\sin^2\theta} = \int_{t_i}^{t_f} dt\ \Omega, \tag{D8b}$$

$$T = \int_{t_i}^{t_f} dt. \tag{D8c}$$

For a bounded pulse $\Omega \leqslant \Omega_0$, optimization with respect to pulse area $\mathcal{A}$ or time T is equivalent in the sense that they provide the same trajectory $\widetilde{\theta}(\gamma)$. Optimization with respect to pulse area $\mathcal{A}$ does not depend on the pulse shape through time reparametrization, while optimization with respect to time (or equivalently to energy) leads to a flat pulse with a constant $\Omega = \Omega_0$, where $T_\mathrm{min} = \mathcal{A}/\Omega_0$.

The optimal trajectory $(\gamma(t), \theta(t))$ can then be determined by the Euler-Lagrange optimization for a fixed QFI, i.e., solution of the Euler-Lagrange equations

$$\frac{\partial\mathcal{L}}{\partial\zeta} - \frac{d}{dt}\left(\frac{\partial\mathcal{L}}{\partial\dot{\zeta}}\right) = 0, \quad \zeta = \gamma, \theta, \tag{D9}$$

for given values of the two integral constraints $\Psi_j(\gamma,\theta) = \Psi_{j,0}$, $j = 1, 2$. The Lagrangian reads

$$\mathcal{L} = \mathcal{L}_0 + \lambda_1\psi_1 + \lambda_2\psi_2, \tag{D10}$$

where λ_j, $j = 1, 2$ are the Lagrange multipliers associated with the two respective constraints Ψ_j, $j = 1, 2$, that can be fixed independently, and

$$\mathcal{E}(\gamma,\theta) = \int_{t_i}^{t_f} dt(\dot{\theta}^2 + \dot{\gamma}^2\sin^2\theta) \equiv \int_{t_i}^{t_f} dt\ \mathcal{L}_0(\dot{\gamma},\theta,\dot{\theta}), \tag{D11}$$

if we consider the minimization of the energy [Eq. (D8a)]. The Euler-Lagrange equations lead to the differential equations of the trajectory $(\gamma(t), \theta(t))$:

$$0 = \ddot{\gamma} + 2\dot{\gamma}\dot{\theta}\cot\theta + \dot{\theta}(\lambda_1\sin\gamma - \lambda_2\cos\gamma), \tag{D12a}$$

$$0 = \ddot{\theta} - \tfrac{1}{2}\dot{\gamma}^2\sin 2\theta - \dot{\gamma}\sin^2\theta(\lambda_1\sin\gamma - \lambda_2\cos\gamma), \tag{D12b}$$

where we have redefined $\lambda_1/2 \to \lambda_1$, $\lambda_2/2 \to \lambda_2$ for convenience.

APPENDIX E: EULER-LAGRANGE EQUATIONS FOR FIFTH-ORDER 0π-NOP

Following this decomposition, the perturbative propagator [Eq. (C1)] can be rewritten as

$$U(t_f,t_i) = U_\Delta(t_f,t_i) \times \begin{bmatrix} 1 + O_1 + O_2 + \cdots & Q_1 + Q_2 + \cdots \\ -(\bar{Q}_1 + \bar{Q}_2 + \cdots) & 1 + \bar{O}_1 + \bar{O}_2 + \cdots \end{bmatrix}, \tag{E1}$$

with $U_\Delta(t,t_i)$ the propagator associated with $H_\Delta(t)$, the perturbative matrix terms [Eq. (C2)], and the perturbation in the interaction representation

$$V_I(t) = U_\Delta^\dagger(t,t_i)V(t)U_\Delta(t,t_i) = \frac{1}{2}\begin{bmatrix} 0 & g(t) \\ \bar{g}(t) & 0 \end{bmatrix}, \quad \text{(E2)}$$

with the function

$$g(t) = \Omega(t)e^{-i\int_{t_i}^t ds\,\Delta(s)} = i\Omega(t)e^{-i\varphi(t)}e^{i\int_{t_i}^t ds\dot{\gamma}(s)\cos\theta(s)}, \quad \text{(E3)}$$

where we have used Eq. (5b). In this case, the fidelity from Eq. (18), around $\alpha=-1$, can be simplified to

$$\begin{aligned}\mathsf{F} &= |\langle\phi_T|\phi_\alpha(t_f)\rangle|^2 = |Q_1+Q_2+\cdots|^2 \\ &= -\widetilde{O}_1-\widetilde{O}_2-\widetilde{O}_3-\cdots\end{aligned} \quad \text{(E4)}$$

with the relation (C6). Since ε is small, we can consider the first terms that read for the considered perturbation (E2):

$$|Q_1| = \varepsilon\left|\int_{t_i}^{t_f} dt\, g(t)\right|, \quad \text{(E5a)}$$

$$Q_2 = 0, \quad \text{(E5b)}$$

$$|Q_3| = \varepsilon^3\left|\int_{t_i}^{t_f} dt\,\bar{g}(t)\left[\int_{t_i}^{t} dt' g(t')\right]^2\right| \text{ when } Q_1=0,$$

$$Q_4 = 0. \quad \text{(E5c)}$$

In this case, one can thus address specifically the derivative at each order of the profile around 0π (i.e., around $\alpha=-1$). We analyze below its explicit realization for the fifth order. The ninth order is treated in Appendix F.

Nullifying $|Q_1|$ around $\alpha=-1$ results in a fifth-order flattening of the profile (in short fifth-order 0π-NOP), because everything up to $\widetilde{O}_5$ included is then nullified according to Eqs. (C6) and (E5). We apply the Euler-Lagrange optimization that minimizes the energy of the pulse with the constraint $|Q_1|=0$. We introduce the dynamical parameter

$$z(t) = \int_{t_i}^{t} ds\,\dot{\gamma}\cos\theta, \quad z(t_i)=0, \quad \dot{z}=\dot{\gamma}\cos\theta, \quad \text{(E6)}$$

in order to take into account the integral in $g(t)$ [Eq. (E3)]. With the use of this parameter, we can reformulate $|Q_1|$ as

$$|Q_1| = \left|\int_{t_i}^{t_f}\varphi_1 dt - i\int_{t_i}^{t_f}\varphi_2 dt\right|, \quad \text{(E7a)}$$

$$\varphi_1(\gamma,\theta,z) = \dot{\gamma}\sin\theta(t)\cos z(t) + \dot{\theta}\sin z(t), \quad \text{(E7b)}$$

$$\varphi_2(\gamma,\theta,z) = \dot{\gamma}\sin\theta(t)\sin z(t) - \dot{\theta}\cos z(t). \quad \text{(E7c)}$$

Therefore, we have to minimize the pulse energy with the following two constraints:

$$\psi_j(\gamma,\theta,z) = \int_{t_i}^{t_f} dt\,\varphi_j(\dot{\gamma},\theta,\dot{\theta},z) = 0,\ j=1,2, \quad \text{(E8)}$$

according to the Lagrangian

$$\mathcal{L} = \mathcal{L}_0(\dot{\gamma},\theta,\dot{\theta}) + \mu_1\varphi_1 + \mu_2\varphi_2 + \mu(t)(\dot{z}-\dot{\gamma}\cos\theta), \quad \text{(E9)}$$

$$\mathcal{L}_0(\dot{\gamma},\theta,\dot{\theta}) = \dot{\theta}^2 + \dot{\gamma}^2\sin^2\theta, \quad \text{(E10)}$$

leading to the four differential equations with four unknown functions to be determined, $\theta(t)$, $\gamma(t)$, $z(t)$, $\mu(t)$:

$$0 = \ddot{\gamma} + 2\dot{\gamma}\dot{\theta}\cot\theta + \frac{1}{2\sin\theta}\mu\dot{\theta}, \quad \text{(E11a)}$$

$$0 = \ddot{\theta} - \dot{\gamma}^2\sin\theta\cos\theta - \frac{1}{2}\mu\dot{\gamma}\sin\theta, \quad \text{(E11b)}$$

$$\dot{\mu} = \mu_1(\dot{\theta}\cos z - \dot{\gamma}\sin\theta\sin z) - \mu_2(\dot{\theta}\sin z + \dot{\gamma}\sin\theta\cos z), \quad \text{(E11c)}$$

$$\dot{z} = \dot{\gamma}\cos\theta \quad \text{(E11d)}$$

forming the NIO Lagrange equations at the fifth order.

APPENDIX F: NINTH-ORDER α-NIO

In this Appendix, we explore the next-order solution by optimal nullification of both Q_1 and Q_3 using Euler-Lagrange optimization. In this case, all of the elements $\widetilde{O}_j$ are nullified for $j\leqslant 9$ according to Eqs. (C6) and (E5). The first step consists in introducing a Lagrangian that takes into account both constraints $|Q_1|=|Q_3|=0$ and the parameter to be minimized (time, energy, or pulse area). For this purpose, we introduce three dynamical parameters:

$$z(t) = \int_{t_i}^{t} ds\,\dot{\gamma}\cos\theta, \quad z(t_i)=0, \quad \dot{z}=\dot{\gamma}\cos\theta, \quad \text{(F1a)}$$

$$y_1(t) = \int_{t_i}^{t}\varphi_1(t')dt', \quad y_1(t_i)=0, \quad \dot{y}_1=\varphi_1(t), \quad \text{(F1b)}$$

$$y_2(t) = \int_{t_i}^{t}\varphi_2(t')dt', \quad y_2(t_i)=0, \quad \dot{y}_2=\varphi_2(t), \quad \text{(F1c)}$$

and therefore $|Q_3|$ becomes

$$|Q_3| = \left|\int_{t_i}^{t_t} dt[\varphi_1(t)+i\varphi_2(t)][y_1(t)-iy_2(t)]^2\right|. \quad \text{(F2)}$$

The Lagrangian writes

$$\begin{aligned}\mathcal{L} = \mathcal{L}_0(\dot{\gamma},\theta,\dot{\theta}) &+ \mu_1\varphi_1 + \mu_2\varphi_2 + \mu_3\mathrm{Re} \\ &\times[(\varphi_1+i\varphi_2)(y_1-iy_2)^2] + \mu_4\Im[(\varphi_1+i\varphi_2)(y_1-iy_2)^2] \\ &+ \mu_5(t)(\dot{z}-\dot{\gamma}\cos\theta) + \mu_6(t)(\dot{y}_1-\varphi_1) + \mu_7(t)(\dot{y}_2-\varphi_2).\end{aligned} \quad \text{(F3)}$$

The terms of the right-hand side of Eq. (F3) account for the optimality and the constraints for nullifying $|Q_1|$ and $|Q_3|$ via the Lagrange multipliers μ_j, $j=1,2,3,4$ and the last three Lagrange multipliers $\mu_k(t)$, $k=5,6,7$ are for the definitions of z, y_1, y_2, respectively. The Lagrangian can be simplified by introducing two variables $\lambda_1(t)$ and $\lambda_2(t)$

$$\begin{aligned}\mathcal{L} = \mathcal{L}_0(\dot{\gamma},\theta,\dot{\theta}) &+ \lambda_1\varphi_1 \\ &+ \lambda_2\varphi_2 + \mu_5(t)(\dot{z}-\dot{\gamma}\cos\theta) + \mu_6(t)\dot{y}_1 + \mu_7(t)\dot{y}_2,\end{aligned} \quad \text{(F4)}$$

with

$$\lambda_1(t) = \mu_1 + \mu_3\left(y_1^2-y_2^2\right) - 2\mu_4 y_1 y_2 - \mu_6(t), \quad \text{(F5a)}$$

$$\lambda_2(t) = \mu_2 + \mu_4\left(y_1^2-y_2^2\right) + 2\mu_3 y_1 y_2 - \mu_7(t). \quad \text{(F5b)}$$

After a similar procedure as before, the set of equations to be solved can be written as

$$2\dot{\gamma}\sin^2\theta + \sin\theta(\lambda_1\cos z - \lambda_2\sin z) - \mu_5(t)\cos\theta = -\mu_{5i}, \tag{F6a}$$

$$2\ddot{\theta} - \dot{\gamma}^2\sin 2\theta - \mu_5(t)\dot{\gamma}\sin\theta + \dot{\lambda}_1\sin z + \dot{\lambda}_2\cos z = 0, \tag{F6b}$$

$$\dot{\mu}_5 = \lambda_1\dot{y}_2 - \lambda_2\dot{y}_1,$$

$$\dot{\lambda}_1 = -4\dot{y}_2(\mu_3 y_2 + \mu_4 y_1),$$

$$\dot{\lambda}_2 = 4\dot{y}_1(\mu_3 y_2 + \mu_4 y_1),$$

$$\dot{z} = \dot{\gamma}\cos\theta, \tag{F6c}$$

$$\dot{y}_1 = \dot{\theta}\sin z + \dot{\gamma}\sin\theta\cos z, \tag{F6d}$$

$$\dot{y}_2 = \dot{\theta}\cos z - \dot{\gamma}\sin\theta\sin z. \tag{F6e}$$

As expected, we obtain that $\Omega(t)$ is constant, $\Omega(t) = \Omega_0$ (chosen positive), which is used for the normalization. The initial values are $\gamma_i = \pi/2$, $\dot{\gamma}_i = -\mu_{5,i}/4$, $\theta_i = 0$, $\dot{\theta}_i = 1$, and $z_i = y_{1,i} = y_{2,i} = 0$. μ_3, μ_4, $\mu_{5,i}$, $\lambda_{1,i}$, $\lambda_{2,i}$ are the free parameters to be determined to satisfy the CPT boundary condition, $\theta_f = \pi$, and the constraints $Q_1 = Q_3 = 0$.

[1] V. Giovannetti, S. Lloyd, and L. Maccone, Quantum-enhanced measurements: Beating the standard quantum limit, Science **306**, 1330 (2004).

[2] V. Giovannetti, S. Lloyd, and L. Maccone, Advances in quantum metrology, Nat. Photon. **5**, 222 (2011).

[3] D. Ma, V. Gulani, N. Seiberlich, K. Liu, J. L. Sunshine, J. L. Duerk, and M. A. Griswold, Magnetic resonance fingerprinting, Nature (London) **495**, 187 (2013).

[4] J. Liu and H. Yuan, Control-enhanced multiparameter quantum estimation, Phys. Rev. A **96**, 042114 (2017).

[5] J. Yang, S. Pang, and A. N. Jordan, Quantum parameter estimation with the Landau-Zener transition, Phys. Rev. A **96**, 020301 (2017).

[6] C. L. Degen, F. Reinhard, and P. Cappellaro, Quantum sensing, Rev. Mod. Phys. **89**, 035002 (2017).

[7] T. Gefen, F. Jelezko, and A. Retzker, Control methods for improved Fisher information with quantum sensing, Phys. Rev. A **96**, 032310 (2017).

[8] F. Poggiali, P. Cappellaro, and N. Fabbri, Optimal control for one-qubit quantum sensing, Phys. Rev. X **8**, 021059 (2018).

[9] Z. Hou, R.-J. Wang, J.-F. Tang, H. Yuan, G.-Y. Xiang, C.-F. Li, and G.-C. Guo, Control enhanced sequential scheme for general quantum parameter estimation at the Heisenberg limit, Phys. Rev. Lett. **123**, 040501 (2019).

[10] L. Liu and H. Yuan, Achieving higher precision in quantum parameter estimation with feedback controls, Phys. Rev. A **102**, 012208 (2020).

[11] D. Basilewitsch, H. Yuan, and C. P. Koch, Optimally controlled quantum discrimination and estimation, Phys. Rev. Res. **2**, 033396 (2020).

[12] P. Rembold, N. Oshnik, M. M. Müller, S. Montangero, T. Calarco, and E. Neu, Introduction to quantum optimal control for quantum sensing with nitrogen-vacancy centers in diamond, AVS Quantum Sci. **2**, 024701 (2020).

[13] S. A. Haine and J. J. Hope, Machine-designed sensor to make optimal use of entanglement generating dynamics for quantum sensing, Phys. Rev. Lett. **124**, 060402 (2020).

[14] H. Xu, L. Wang, H. Yuan, and X. Wang, Generalizable control for multiparameter quantum metrology, Phys. Rev. A **103**, 042615 (2021).

[15] J. Liu, M. Zhang, H. Chen, L. Wang, and H. Yuan, Optimal scheme for quantum metrology, Adv. Quantum Tech. **5**, 2100080 (2022).

[16] J. Yang, S. Pang, Z. Chen, A. N. Jordan, and A. del Campo, Variational principle for optimal quantum controls in quantum metrology, Phys. Rev. Lett. **128**, 160505 (2022).

[17] C. Lin, Y. Ma, and D. Sels, Application of Pontryagin's maximum principle to quantum metrology in dissipative systems, Phys. Rev. A **105**, 042621 (2022).

[18] M. Zhang, H.-M. Yu, H. Yuan, X. Wang, R. Demkowicz-Dobrzanski, and J. Liu, QuanEstimation: An open-source toolkit for quantum parameter estimation, Phys. Rev. Res. **4**, 043057 (2022).

[19] Y. Zhai, X. Yang, K. Tang, X. Long, X. Nie, T. Xin, D. Lu, and J. Li, Control enhanced quantum metrology under Markovian noise, Phys. Rev. A **107**, 022602 (2023).

[20] J. T. Reilly, J. D. Wilson, S. B. Jäger, C. Wilson, and M. J. Holland, Optimal generators for quantum sensing, Phys. Rev. Lett. **131**, 150802 (2023).

[21] J. C. Pelayo, K. Gietka, and T. Busch, Distributed quantum sensing with optical lattices, Phys. Rev. A **107**, 033318 (2023).

[22] K. Herb and C. L. Degen, Quantum speed limit in quantum sensing, Phys. Rev. Lett. **133**, 210802 (2024).

[23] D. Louzon, G. T. Genov, N. Staudenmaier, F. Frank, J. Lang, M. L. Markham, A. Retzker, and F. Jelezko, Robust noise suppression and quantum sensing by continuous phased dynamical decoupling, Phys. Rev. Lett. **134**, 120802 (2025).

[24] S. Pang and A. N. Jordan, Optimal adaptive control for quantum metrology with time-dependent Hamiltonians, Nat. Commun. **8**, 14695 (2017).

[25] M. Naghiloo, A. N. Jordan, and K. W. Murch, Achieving optimal quantum acceleration of frequency estimation using adaptive coherent control, Phys. Rev. Lett. **119**, 180801 (2017).

[26] J. Liu and H. Yuan, Quantum parameter estimation with optimal control, Phys. Rev. A **96**, 012117 (2017).

[27] D. Guéry-Odelin, A. Ruschhaupt, A. Kiely, E. Torrontegui, S. Martínez-Garaot, and J. G. Muga, Shortcuts to adiabaticity: Concepts, methods, and applications, Rev. Mod. Phys. **91**, 045001 (2019).

[28] U. Boscain, M. Sigalotti, and D. Sugny, Introduction to the Pontryagin maximum principle for quantum optimal control, PRX Quantum **2**, 030203 (2021).

[29] D. Stefanatos and E. Paspalakis, A shortcut tour of quantum control methods for modern quantum technologies, Europhys. Lett. **132**, 60001 (2020).

[30] C. P. Koch, U. Boscain, T. Calarco, G. Dirr, S. Filipp, S. Glaser, R. Kosloff, S. Montangero, T. Schulte-Herbruggen, D. Sugny, and F. K. Wilhelm, Quantum optimal control in quantum technologies, strategic report on current status, visions and goals for research in Europe, EPJ Quantum Technol. **9**, 19 (2022).

[31] Q. Ansel, E. Dionis, F. Arrouas, B. Peaudecerf, S. Guérin, D. Guéry-Odelin, and D. Sugny, Introduction to the theoretical and experimental aspects of quantum optimal control, J. Phys. B **57**, 133001 (2024).

[32] M. Cabedo-Olaya, J. G. Muga, and S. Martínez-Garaot, Shortcut-to-adiabaticity-like techniques for parameter estimation in quantum metrology, Entropy **22**, 1251 (2020).

[33] C. Lin, Y. Ma, and D. Sels, Optimal control for quantum metrology via Pontryagin's principle, Phys. Rev. A **103**, 052607 (2021).

[34] Q. Ansel, E. Dionis, and D. Sugny, Optimal control strategies for parameter estimation of quantum systems, SciPost Phys. **16**, 013 (2024).

[35] J. Liu *et al.*, Quantum Fisher information matrix and multiparameter estimation, J. Phys. A: Math. Theor. **53**, 023001 (2020).

[36] Q. Ansel, M. Tesch, S. J. Glaser, and D. Sugny, Optimizing fingerprinting experiments for parameter identification: Application to spin systems, Phys. Rev. A **96**, 053419 (2017).

[37] S. L. Braunstein and C. M. Caves, Statistical distance and the geometry of quantum states, Phys. Rev. Lett. **72**, 3439 (1994).

[38] IBM Quantum, https://quantum.cloud.ibm.com/.

[39] G. Aleksandrowicz *et al.*, Qiskit: An open-source framework for quantum computing, Zenodo (2019), https://doi.org/10.5281/zenodo.2562111.

[40] T. Alexander, N. Kanazawa, D. J. Egger, L. Capelluto, C. J. Wood, A. Javadi-Abhari, and D. McKay, Qiskit pulse: Programming quantum computers through the cloud with pulses, Quantum Sci. Technol. **5**, 044006 (2020).

[41] N. V. Vitanov, Arbitrarily accurate narrowband composite pulse sequences, Phys. Rev. A **84**, 065404 (2011).

[42] D. Daems, A. Ruschhaupt, D. Sugny, and S. Guérin, Robust quantum control by a single-shot shaped pulse, Phys. Rev. Lett. **111**, 050404 (2013).

[43] G. Dridi, K. Liu, and S. Guérin, Optimal robust quantum control by inverse geometric optimization, Phys. Rev. Lett. **125**, 250403 (2020).

[44] M. Harutyunyan, F. Holweck, D. Sugny, and S. Guérin, Digital optimal robust control, Phys. Rev. Lett. **131**, 200801 (2023).

[45] O. Fresse-Colson, S. Guérin, X. Chen, and D. Sugny, Application of the Pontryagin maximum principle to the robust time-optimal control of two-level quantum systems, Phys. Rev. A **112**, 022618 (2025).

[46] U. Boscain, G. Charlot, J.-P. Gauthier, S. Guérin, and H. R. Jauslin, Optimal control in laser-induced population transfer for two- and three-level quantum systems, J. Math. Phys. **43**, 2107 (2002).

[47] B. T. Torosov and N. V. Vitanov, Experimental demonstration of composite pulses on IBM's quantum computer, Phys. Rev. Appl. **18**, 034062 (2022).

[48] T. Monz, K. Kim, W. Hänsel, M. Riebe, A. S. Villar, P. Schindler, M. Chwalla, M. Hennrich, and R. Blatt, Realization of the quantum Toffoli gate with trapped ions, Phys. Rev. Lett. **102**, 040501 (2009).

[49] C. Weitenberg, M. Endres, J. F. Sherson, M. Cheneau, P. Schauss, T. Fukuhara, I. Bloch, and S. Kuhr, Single-spin addressing in an atomic mott insulator, Nature (London) **471**, 319 (2011).

[50] S. S. Ivanov and N. V. Vitanov, High-fidelity local addressing of trapped ions and atoms by composite sequences of laser pulses, Opt. Lett. **36**, 1275 (2011).

[51] E. Kyoseva and N. V. Vitanov, Arbitrarily accurate passband composite pulses for dynamical suppression of amplitude noise, Phys. Rev. A **88**, 063410 (2013).